Structural, electrical, and optical properties of $La_{1-z}Y_zH_x$ switchable mirrors

A. T. M. van Gogh, D. G. Nagengast, E. S. Kooij, N. J. Koeman, J. H. Rector, and R. Griessen
Faculty of Sciences, Division of Physics and Astronomy, Vrije Universiteit, De Boelelaan 1081, 1081 HV Amsterdam, The Netherlands

C. F. J. Flipse and R. J. J. G. A. M. Smeets
Department of Applied Physics, Physics of Surfaces and Interfaces, Eindhoven University of Technology, 5600 MB Eindhoven, The Netherlands

(Received 15 August 2000; revised manuscript received 6 November 2000; published 20 April 2001)

Thin $La_{1-z}Y_zH_x$ films, in the composition range $0<z<1$ and $0<x<3$, are studied using x-ray diffraction, dc resistivity measurements, reflectance-transmittance measurements, and ellipsometry in the visible and near-infrared spectral range. For $x=0$ the structural phase diagram is similar to that of the bulk system. Upon hydrogen absorption and desorption, the $La_{1-z}Y_zH_x$ films do not disproportionate. All dihydrides have a fcc structure with a continuous shift of the lattice parameter, whereas the trihydrides undergo a transition from a fcc lattice structure for $0<z<0.67$ to a hexagonal lattice structure for $0.81<z<1$. No significant thin-film effects occur in the structural, electrical, and optical properties, whereas disorder effects are observed in the x-ray coherence length, the electron relaxation time at both zero and optical frequencies, and in the optical properties of the trihydrides. In LaH_2 a similar dihydride transmission window is observed as in YH_2. The suppression of this window upon alloying is a disorder effect. As in the case of their parent materials, all $La_{1-z}Y_zH_x$ alloys (both cubic and hexagonal) exhibit a metal-insulator transition for $2<x<3$, which is a clear demonstration of the robustness of the metal-insulator transition in switchable mirrors. The optical band-gap shifts from 1.87 ± 0.03 eV for LaH_3 to 2.63 ± 0.03 eV for YH_3. The optical properties suggest that the fundamental band gap is 1–1.8 eV lower.

DOI: 10.1103/PhysRevB.63.195105 PACS number(s): 71.30.+h, 61.66.Dk, 73.61.−r, 78.20.−e

I. INTRODUCTION

Switchable metal hydrides have received much attention since 1996, when Huiberts *et al.*[1] discovered that the optical properties of thin films of Y and La exhibit drastic changes under exposure of hydrogen. In these films the hydrogen concentration x can be changed from 0 to 3 at room temperature by applying H_2 gas at moderate pressures ($\lesssim 10^5$ Pa). When x increases from 2 to 3 the material changes from a reflective metal into a transparent insulator. Shortly afterwards it was shown that not only Y and La but most rare-earth (RE) metals exhibit such a metal-insulator transition.[2] In addition, by using RE-based alloys the optical properties can be tuned.[2–4] This, together with the fact that H loading and unloading of these films is reversible and can also be done electrochemically,[5,6] make these metal-hydride systems technologically interesting. However the Y and La hydride systems are also very interesting from a fundamental point of view. Before 1997 state-of-the-art band-structure calculations on YH_3 and LaH_3 predicted a metallic ground state of these materials. Since 1997 several theoretical calculations came up with explanations of why ordinary band-structure calculations failed,[7–11] and experimental work was done to elucidate why trihydrides are insulators.[12,13] Although progress has been made, the physical mechanism underlying the metal-insulator (MI) transition is still under debate.

In this work we present a systematic study of $La_{1-z}Y_zH_x$ thin films. Yttrium and lanthanum are chemically very similar, both having a d^1s^2 valence configuration. This similarity is reflected in the simplicity of the (bulk) phase diagram of the $La_{1-z}Y_z$ system. The two metals form a solid solution over almost the whole composition range. For $z<0.4$ the alloys have a La double hexagonal close packed (dhcp) structure, and for $z>0.6$ a Y (hcp) structure.[14] However, YH_x and LaH_x behave quite differently for x between 2 and 3: YH_x changes from a fcc structure to a hexagonal lattice structure with a large increase in atomic volume, whereas LaH_x stays fcc with a small decrease of atomic volume upon hydrogenation.

We show that La-Y alloys do not disproportionate upon hydrogenation, as is the case, for example, in the Y-Mg system,[4] which makes the La-Y system particularly suitable for studying the influence of lattice structure, lattice parameters, and microscopic disorder on various physical quantities. We also show that a MI-transition occurs in all alloys regardless of their crystal structure (cubic or hexagonal).

After Sec. II, a short explanation of the MI transition in the $La_{1-z}YzH_x$ system is given. We then focus on the lattice structure of $La_{1-z}Y_zH_x$ thin films. This information is used in the interpretation of later results that are mainly concerned with electrical and optical properties of $La_{1-z}Y_zH_x$.

II. EXPERIMENT

A. Samples

$La_{1-z}Y_z$ films of 300-nm thickness are made at room temperature and under ultrahigh-vacuum conditions ($\sim 10^{-8}$ Pa) by *e*-gun codeposition of the parent metals (99.9% purity). The films are evaporated on quartz glass substrates (Suprasil™ plaquettes and Herasil™ prisms, Heraeus), and are covered by a thin cap layer to protect the highly reactive La-Y layer against oxidation and to catalyze the dissociation of H_2 molecules. For $z>0.5$ this cap layer consists of 15-nm Pd. For $z<0.5$ we use a composite AlO_x/Pd cap

layer, consisting of 1.5-nm AlO_x subsequently covered with 15-nm Pd. As shown by van Gogh *et al.*,[15] simply covering La-rich films with 15-nm Pd does not prevent them from oxidation, because of the strong Pd diffusion into the underlying La layer. However, a 1.5-nm layer of AlO_x effectively prevents this process. The Pd layer remains necessary because AlO_x does not act as a catalyst for H_2 dissociation. In every evaporation run three identical samples are made: one is used for simultaneous x-ray diffraction (XRD) and resistivity measurements. The second sample is used for simultaneous optical and resistivity measurements. A third sample is used for composition and thickness measurements using Rutherford backscattering (RBS) and profilometry, respectively. These measurements have shown that *z* values have an accuracy of 2 at. %. Film thicknesses are accurate to 2%, and values obtained from RBS and profilometry agree within experimental accuracy. We found oxygen contaminations of a few at. %.

B. X-ray diffraction

X-ray diffraction on a series of La-Y alloys is done using a RIGAKU diffractometer. The sample is mounted in a gas cell with Be windows to enable *in situ* hydrogenation. Data are collected every 0.04° over a 2θ angular range of 20°–70°, with integration times varying between 10 and 20 s. The incident angle θ is kept fixed at 10° to optimize the probed volume. In this way many Bragg reflections are measured, optimizing the structural information. For each sample we measure the as-deposited film, after which we apply 10^5 Pa of H_2 gas. Subsequently, a trihydride spectrum is measured. The film is then taken out of the system and is put in an oven for 1 h at 100 °C to ensure desorption back to the dihydride state. The sample is mounted back in the gas cell and a dihydride spectrum is measured. To check reproducibility the film is again loaded to the trihydride phase, and a second trihydride spectrum is measured.

C. Optical properties and dc resistivity

The optical properties for the as-deposited metal films and the (metallic) dihydride are determined by ellipsometry and reflectance-transmittance (*R*-*T*) measurements. For ellipsometry, we use a rotating analyzer ellipsometer (VASE, J. A. Woollam Co., Inc.) that measures the ratio of the complex Fresnel reflection coefficients

$$\frac{R_p}{R_s} = \tan\Psi \exp i\Delta \tag{1}$$

in terms of the ellipsometric quantities $\Psi(\omega)$ and $\Delta(\omega)$ in the spectral range $0.75 \leqslant \hbar\omega \leqslant 4.5$ eV. The subscripts refer to polarizations parallel (*p*) and perpendicular (*s*) to the plane of incidence. As the Pd cap layer is strongly absorbing, we measure the optical properties through the substrate. With flat substrates there are difficulties in inverting the measured data into the (complex) dielectric function $\varepsilon(\omega)$. The reason for this is that substrates are macroscopically thick ($\sim$1 mm), so that the reflected light from the air/quartz interface is spatially separated at the detector position from the reflected light coming from the quartz/$La_{1-z}Y_zH_x$ interface. To circumvent this problem we have used, as substrates, quartz glass prisms with a top angle of 40° (see Fig. 1). The angle of incidence is set at 70 °, and the light from the air/quartz interface is no longer reflected directly in the direction of the detector. Another advantage is that because of the perpendicular angle of incidence at the air/quartz interfaces no polarization changes occur at these interfaces. In the numerical inversion of Ψ and Δ the substrate therefore acts as an ambient, and not as part of the multilayer stack. Both advantages make the method very accurate ($\approx$5%) when the $La_{1-z}Y_zH_x$ layer is metallic. A disadvantage is that Ψ and Δ cannot be measured under different angles. This makes the prism method less accurate for transparent samples.

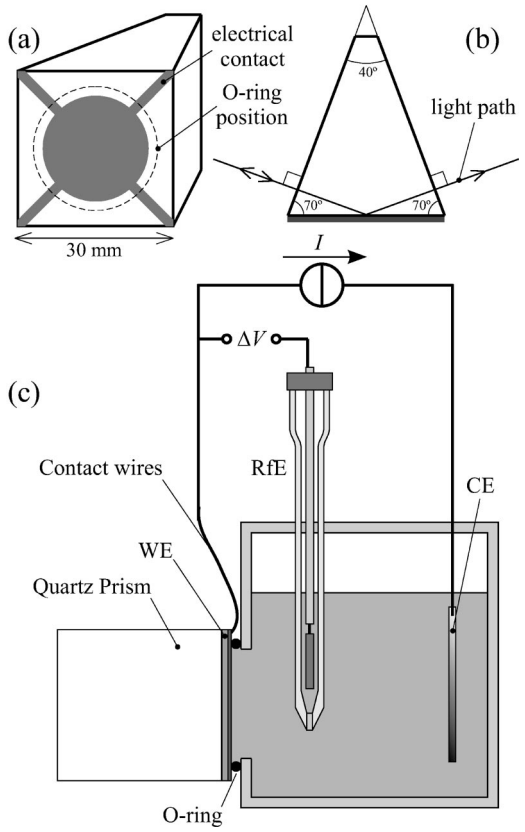

FIG. 1. Geometry of the samples used for ellipsometry. The dashed line in (a) indicates the position of the *O* ring when the prism is mounted in the electrochemical loading cell. The four stripes are used as electrical contacts. In (b) the light path is indicated during ellipsometry. (c) Schematic side view of the electrochemical cell used for potentiostatic loading of the $La_{1-z}Y_zH_x$ alloys. We used the abbreviation WE for the working electrode ($La_{1-z}Y_zH_x$), RfE for the reference electrode, and CE for the counterelectrode.

As there are more than two interfaces, no analytical functions exist between $\Psi(\omega)$ and $\Delta(\omega)$ and the unknown dielectric function $\varepsilon(\omega)$ of the $La_{1-z}Y_zH_x$ layer. To obtain $\varepsilon(\omega)$ numerically we use the program WVASE (J. A. Woollam Co., Inc.), which takes as input the measured $\Psi(\omega)$ and $\Delta(\omega)$, the thicknesses of the various layers of the stack and the dielectric functions of the substrate, the Pd layer, and the AlO_x layer. For optically thick films, e.g., 300-nm metallic

$La_{1-z}Y_zH_x$ films, ellipsometry is easier and more accurate than R-T measurements. However, when the films become optically thin, e.g., 300-nm $La_{1-z}Y_zH_x$ films in their transparent state, the numerical inversion of Ψ and Δ becomes less accurate and not unique. This is one of the reasons for performing R-T measurements.

The prism is mounted in a teflon electrochemical cell consisting of a reservoir filled with 1-M KOH electrolyte solution, a Hg/HgO reference electrode (RfE), and a Pt counter electrode (CE) as sketched in Fig. 1(c). The $La_{1-z}Y_z$ film acts as a working electrode (WE), and is connected to the potentiostat via the four stripes indicated in Fig. 1(a). During electrochemical loading, the four wires are interconnected for optimal homogeneous loading. The hydrogen concentration x is varied potentiostatically using a Wenking POS 73 potentiostat. At time t_1 a current $i(t)$ is forced to flow between the WE and CE such that the potential ΔV between the RfE and the WE reaches a certain value. At the working electrode the following reaction takes place:

$$H_2O + e^- \rightarrow H_{ad} + OH^-, \tag{2}$$

and subsequently the adsorbed hydrogen atom H_{ad} is absorbed by the switchable mirror. The equivalent hydrogen pressure p_{H_2} is related to ΔV by the Nernst equation

$$\ln p_{H_2} = -\frac{2F}{RT}(\Delta V + 0.926\ \mathrm{V}), \tag{3}$$

in which R is the molar gas constant, F the Faraday constant ($=96\,485.309\ \mathrm{C\,mol^{-1}}$), and T is the temperature. Hence determining $\Delta V(x)$ is equivalent to measuring the pressure-composition (p-x) isotherm. After the system reaches diffusive equilibrium, typically after $\Delta t = 1800$ s, the hydrogen concentration x can be determined using

$$\Delta x = -\frac{V_m}{AdF}\int_t^{t+\Delta t}[i(t') - i_{leak}]dt', \tag{4}$$

in which V_m is the molar volume of the La-Y material under consideration, A is the sample area, d the film thickness, and i_{leak} is the leak current.

Electrochemical loading is done while the cell is mounted on the ellipsometer. After the sample reaches equilibrium, a spectrum is measured. Subsequently the four contacts [see Fig. 1(a)] are reconnected to a resistivity ρ measuring circuit. We use a Keithley 2000 multimeter equipped with a 2000-SCAN scanner card, with which the four wires can be reconnected quickly. Accurate ρ values are obtained by using the van der Pauw method.[16] The hydrogen loss during a resistivity measurement, which takes ~ 1 s, is negligible. By repeating this procedure we obtain the optical constant ρ as a function of x and the pressure-composition (p-x) isotherm.

It turns out that the first loading is inhomogeneous, whereas subsequent loadings are homogeneous and reproducible. Therefore the fresh sample is always switched to a trihydride and back to a dihydride before actual measurements are done. Note that at room temperature the sample cannot be desorbed further than the dihydride.

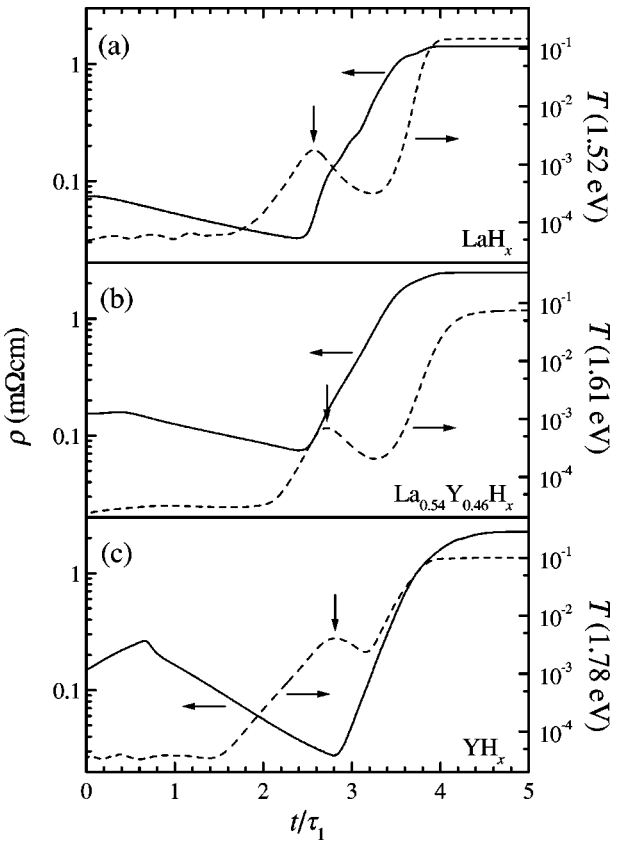

FIG. 2. Time dependence of the optical transmittance and dc resistivity for LaH_x, $La_{0.54}Y_{0.46}H_x$, and YH_x after 1000 mbar of H_2 is applied at $t=0$. The transmittance is plotted for each material for the photon energy for which the dihydride transmittance window (indicated by a vertical arrow) is maximum. To compare the results, the time is scaled by the switching time τ_1 defined in the text. The switching times in (a), (b), and (c) are 20.5, 14.8, and 15.8 s, respectively.

For reflectance transmittance measurements we use flat substrates ($7.5\times10\times1\ \mathrm{mm^3}$). After deposition electrical contacts are made using ultrasonic bonding of 30-μm-thick aluminum wires. Subsequently the film is mounted in a gas loading cell placed into a Bruker IFS 66/S Fourier-transform infrared spectrometer equipped with a reflection/transmission accessory. During H_2 gas loading at $\sim 10^4$ Pa, transmittance and (near-normal-incidence) reflectance spectra are measured alternately ($0.72\ \mathrm{eV} < \hbar\omega < 3.5\ \mathrm{eV}$), and at the same time the resistivity ρ of the film is measured continuously using the van der Pauw method. The H_2 gas pressure is chosen low enough to ensure that the film is in quasiequilibrium during one R-T measurement cycle, which takes about 30 s. After stabilization of the optical reflectance, transmittance and resistivity, the pressure is increased stepwize toward 10^5 Pa.

III. RESULTS AND DISCUSSION

A. Metal-insulator transition in $La_{1-z}Y_zH_x$

In Fig. 2 the evolution of the dc resistivity and the optical transmittance is shown after a hydrogen pressure of $\sim 10^4$ Pa

is applied at a time $t=0$. Results are shown for LaH_x, YH_x and $La_{0.54}Y_{0.46}H_x$. Note that a comparison of the $\rho(t)$ curve with $\rho(x)$, as measured by Kooij *et al.*,[6] shows that x increases roughly linearly with time.

The qualitative behavior of the three materials shown in Fig. 2 (and of all other alloys) is the same. In order to compare the curves, they are scaled to the switching time τ_i for the ith loading, defined as the time between the minimum resistivity $\rho_{\min}$ near $x=2$, and $\rho=\rho_{\min}+1/2(\rho_{\text{final}}-\rho_{\min})$, with ρ_{final} the saturation value. The switching times for the first loading are of the order of 100 s, and are discussed later. Initially ρ rises because of impurity scattering by the added H atoms. This initial rise is observed for all alloys, although the rise in ρ becomes smaller for smaller z. This is due to the fact that the α-β phase boundary occurs at lower x for LaH_x than for YH_x (at $x=0.01$ and 0.24, respectively).[17] After a certain time a low-resistivity β-phase dihydride precipitates into the α-phase matrix. This causes a continuous lowering of ρ.

When x approaches 2, the resistivity is minimal. In a simple picture at $x=2$ all tetrahedral positions (two per metal atom) are filled and all octahedral positions (one per metal atom) are empty. A minimum in resistivity is then expected, because of minimal disorder. However, in practice premature octahedral filling (i.e., filling of the octahedral positions for $x<2$) can occur. In bulk LaH_x it is observed[18] to happen at $x=1.95$. Weaver *et al.*[19] concluded from optical measurements and band-structure calculations that premature octahedral filling occurs in bulk YH_x between $x=1.7$ and 1.9. Inelastic neutron scattering,[20] neutron powder diffraction,[21] and nuclear magnetic resonance[22] yielded octahedral fillings of 8–16 % for bulk $YH_{2.0}$. These results are consistent with the minimum in resistivity at $x=1.8$, observed by Kooij *et al.*[6] for polycrystalline YH_x *films*.

The premature filling of the octahedral positions decreases gradually for lower z. The dihydride resistivities are 2–6 times smaller than the resistivity of the as-deposited films.

After the material has fully transformed into the β phase, the resistivity increases steeply. In this region the transmittance of the film also increases strongly. Between $x=2$ and 3 the film changes from a low-resistivity metal into a transparent insulator. As will be shown later, for $z>0.81$ another structural phase transition takes place in this region, resulting in the γ phase precipitating within the β-phase matrix. However, for $z<0.67$ the same steep increase of ρ and T is observed, clearly indicating that the MI transition is not driven by a structural phase transition. We thus find that a similar MI transition occurs for all $La_{1-z}Y_z$ alloys, showing the robustness of the MI transition and its electronic (i.e., nonstructural) origin.

In the following sections we report on a systematic study of the structural, optical, and electrical properties for $x=0$, 2, and 3. Note that these integer values for x are only used to indicate the as-deposited alloy films of $La_{1-z}Y_z$, and their dihydrides and trihydrides. In fact, we know from independent investigations that the as-deposited films contain x

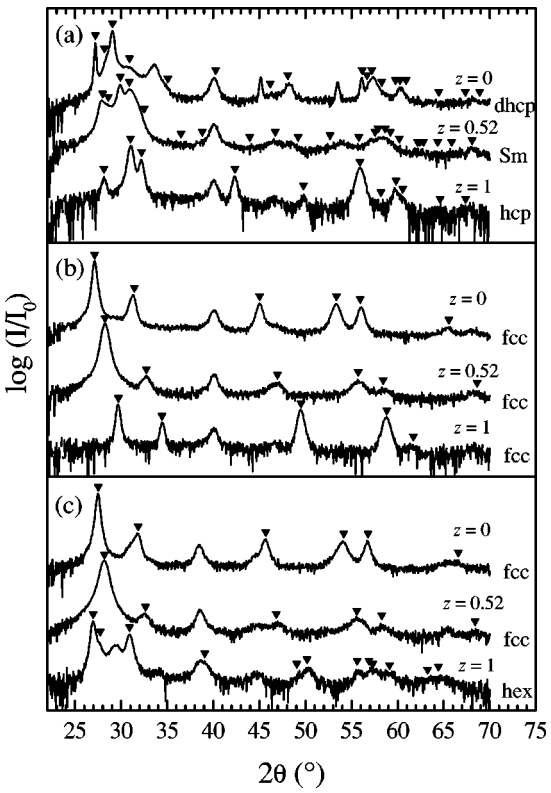

FIG. 3. X-ray-diffraction spectra of $La_{1-z}Y_zH_x$ with $z=0$, 0.52, and 1 for (a) the as-deposited films ($x=0$); (b) the dihydrides ($x=2$); and (c) the trihydrides ($x=3$). The spectra were corrected for the amorphous substrate by subtracting from the raw spectra the spectrum of a plain substrate times a constant of the order 1. The triangles indicate the peak positions for the structure indicated at the right of each spectrum. The other peaks are discussed in the text.

≈ 0.16 hydrogen. The dihydrides have $x\approx 1.9$. The hydrides have a composition close to 2.9 under 10^5 Pa of H_2 gas at room temperature.

B. Structure of $La_{1-z}Y_zH_x$

1. Structure of as-deposited films

Figure 3 shows XRD spectra for $x=0$, 2, and 3 for three $La_{1-z}Y_zH_x$ alloys. Similar results were obtained for all other alloys.

The structure and the lattice parameters for the as-deposited films are listed in Table I, and shown in Fig. 4. To compare the c axes we used reduced values for the dhcp and the Sm structured films: $c=c_{\text{dhcp}}/2$ and $c=2c_{\text{Sm}}/9$.

The narrow peaks at 27°, 45°, 53°, and 56° for the La spectrum ($z=0$) in Fig. 3(a) are precipitations of LaH_2. The broad peak at 33.6° corresponds to fcc-La, that is known[23] to form at a rather low temperature of 583 K. It might be formed during deposition due to sample heating by radiation from the metal sources.

Figure 3(a) shows five peaks between 25° and 35° for the $La_{0.48}Y_{0.52}$ alloy, which is characteristic of the Sm structure (hcp and dhcp give three and four peaks, respectively). However, the peak at 54.23° is characteristic of hcp material. We

TABLE I. Structural properties of $La_{1-z}Y_z$. Values for the c axis are reduced values, i.e., for hcp $c=c_{hcp}$, for dhcp $c=c_{dhcp}/2$, and for Sm $c=2c_{Sm}/9$. The molar volume V_m is per mole of metal atoms.

z	Structure	a (Å)	c (Å)	V_m (cm^3/mol)
0	dhcp	3.769	6.102	22.60
0.15	dhcp	3.714	6.068	21.82
0.21	dhcp	3.697	6.059	21.59
0.30	dhcp	3.698	5.992	21.37
0.46	Sm	3.686	5.911	20.94
0.52	hcp+Sm	3.690	5.933	21.07
0.67	hcp	3.689	5.850	20.76
0.86	hcp	3.678	5.793	20.44
1	hcp	3.648	5.732	19.89

thus conclude that the $La_{0.48}Y_{0.52}$ alloy is in a Sm-hcp mixed phase.

The values given in Table I have been corrected for H incorporation during evaporation, caused by rest H_2 gas in the molecular-beam-epitaxy system partly coming from the release of H_2 due to heating of the Y and La targets during film deposition. By making a linear fit to literature values of a and c for α^*-YH_x, with x between 0 and 0.22,[17,23] we find (in Å) $a(x)=3.6482+0.073\times x$ and $c(x)=5.7318+0.284\times x$ and from this an initial concentration $x=0.16\pm0.03$ for the as-deposited Y. To correct for the native H concentration all values are multiplied with correction factors 3.6482/3.662 (for the a axes) and 5.770/5.7318 (for the c axes), which make the measured values for Y equal to their literature values.[23] Using these factors the experimental La values also correspond to the literature values, which justifies the correction method.

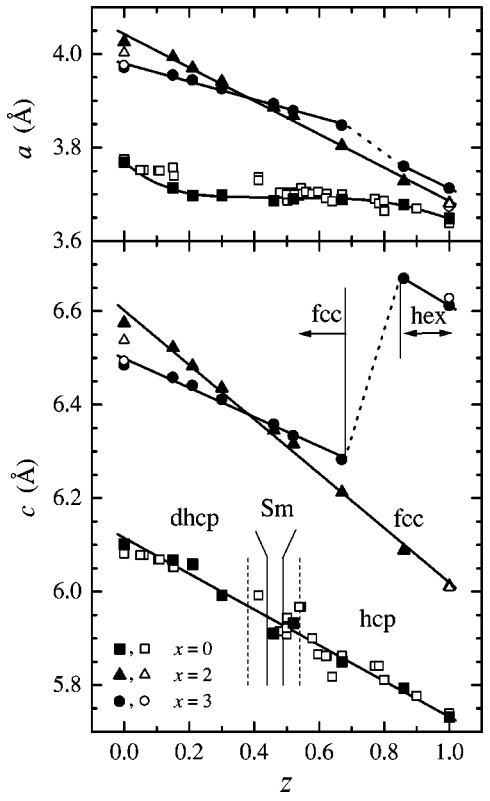

FIG. 4. Composition dependence of the lattice parameters of $La_{1-z}Y_zH_x$ for the as-deposited films ($x=0$) and for the dihydrides and trihydrides ($x=2$ and 3, respectively). The open symbols are literature values (Refs. 14, 23, 36). Vertical lines indicate the phase boundaries for the various structural phases (solid lines) and mixed-phase regions (dashed lines).

Note that the experimental values for Y are within 2% of those obtained from total energy calculations[24] for hcp-Y: $a=3.58$ Å and $c=5.73$ Å . To our knowledge values for La were never calculated, one reason being the complexity of including f electrons in the calculations.

As far as the lattice parameters are concerned, the as-deposited thin films behave like their bulk counterparts. However, the phase boundaries (see Fig. 4) of the Sm-phase have shifted 0.065 to lower z values compared to the boundaries proposed by Gschneidner *et al.*[14] Such differences are also found among bulk data sets and are therefore probably not significant.

In RE metals and RE binary alloys a strong correlation exists between the c/a ratio and the observed lattice structure:[25,26] $c/a<1.6$ for hcp, and $1.6\leqslant c/a<1.606$ for Sm, and $1.606\leqslant c/a<1.633$ for dhcp. It turns out that for $z\geqslant0.46$ the experimental lattice structures for the as-deposited films correspond well with those expected from the measured c/a ratios. Although the ratio is large for the $z=0.52$ alloy, it falls within the scatter of the bulk values.[14] The dhcp alloys ($0.15\leqslant z<0.30$) have c/a ratios that are significantly larger than their bulk counterparts,[14] with a maximum value of 1.639 for $z=0.21$. Figure 4 shows that the large c/a ratio is mainly due to compressed a axes, and to a lesser extent to expanded c axes for $0.15\leqslant z<0.30$. This points to a clamping effect. All films show a preferred orientation with their c axes perpendicular to the substrate. Tensile strains within the hexagonal planes, due to substrate clamping, result in a decrease of a and consequently in an increase of c.

2. Structure of dihydride films

Table II shows that all dihydrides have the fcc lattice structure. The fcc structure differs from the hexagonal structures hcp, dhcp and Sm only in the stacking of hexagonal planes: *ABCABC* . . . for fcc, *ABABA* . . . for hcp, *ABACA* . . . for dhcp, and *ABABCBCACA* . . . for Sm. Therefore, we can compare the lattice parameters for the dihydride films with those for $x=0$ and 3, by defining $a=a_{fcc}/\sqrt{2}$ and $c=2a_{fcc}/\sqrt{3}$. Figure 4 shows that, for $x=2$, the alloys fulfill Vegard's law, that is, the lattice parameters shift linearly between the LaH_2 and YH_2 values. The volume expansion is about 23% for $z=0$ and 7% for $z=1$ (see Fig. 5). Note that the measured lattice parameters for YH_2 agree within 0.2% with values obtained from total energy calculations by Wang and Chou.[29] The agreement with theoretical values is better for YH_2 than for Y, probably because d electrons that are present in Y, give relatively large exchange correlation effects that are not properly included in local-

TABLE II. Structural properties of $La_{1-z}Y_zH_2$. To compare the fcc lattice parameters with those for the hexagonal structures, we defined $a := a_{fcc}/\sqrt{2}$ and $c := 2a_{fcc}/\sqrt{3}$.

z	Structure	a_{fcc} (Å)	a (Å)	c (Å)	V_m (cm^3/mol)
0	fcc	5.694	4.026	6.575	27.79
0.15	fcc	5.648	3.994	6.522	27.13
0.21	fcc	5.614	3.970	6.482	26.64
0.30	fcc	5.573	3.941	6.435	26.06
0.46	fcc	5.495	3.886	6.345	24.98
0.52	fcc	5.470	3.868	6.316	24.64
0.67	fcc	5.380	3.804	6.212	23.44
0.86	fcc	5.273	3.729	6.089	22.07
1	fcc	5.206	3.681	6.011	21.24

density-approximation calculations.[24] In the latter reference it is shown that the lattice expansion going from Y to YH_2 is driven by lowering of the kinetic energy between the tetrahedral H atoms and the metal atoms.

3. Structure of trihydride films

XRD results for $x \approx 3$ are summarized in Table III. Figure 4 shows that the trihydrides fulfill Vegard's law within the fcc phase. For $z > 0.86$ we have too few points to conclude on this matter.

For $z > 0.86$ the films undergo a large uniaxial c-axis expansion of $9.7 \pm 0.2\%$ when x changes from 2 to 3, which causes the extraordinary large c/a ratio for $z \geqslant 0.86$ and $x \approx 3$. This strong uniaxial expansion causes large hysteresis

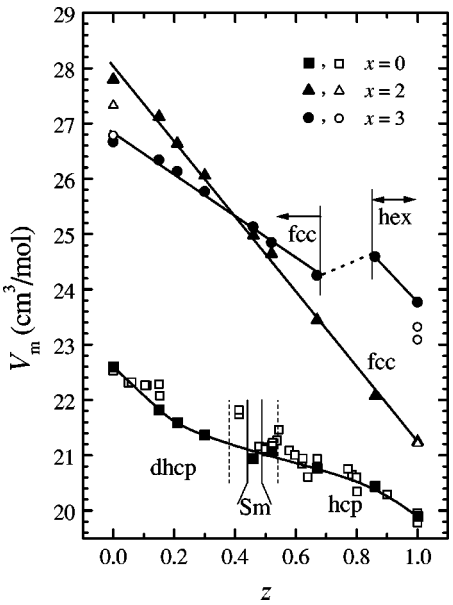

FIG. 5. Molar volume of $La_{1-z}Y_z$ as a function of z. The as-deposited films show no significant deviations from values obtained for bulk material. Solid vertical lines indicate the phase boundaries for the different structural phases. Dashed vertical lines indicate mixed-phase regions. Open symbols indicate literature values (Refs. 14, 27, 28).

TABLE III. Structural properties for $La_{1-z}Y_zH_3$. For the definitions of a_{fcc}, a, c, and V_m see Tables I and II.

z	Structure	a_{fcc} (Å)	a (Å)	c (Å)	V_m (cm^3 /mol)
0	fcc	5.616	3.971	6.485	26.67
0.15	fcc	5.593	3.955	6.458	26.34
0.21	fcc	5.578	3.944	6.441	26.13
0.30	fcc	5.552	3.926	6.411	25.77
0.46	fcc	5.506	3.893	6.358	25.13
0.52	fcc	5.485	3.878	6.334	24.84
0.67	fcc	5.441	3.847	6.283	24.25
0.86	hex	–	3.760	6.670	24.59
1	hex	–	3.713	6.612	23.77

effects in the optical, electrical, and structural properties between the dihydride and trihydride.[30,31]

The large uniaxial expansion can be understood qualitatively as follows. In the ideal hcp structure, two H atoms per Y atom occupy the tetrahedral interstitial sites (H_{tet}) and one H atom the octahedral site (H_{oct}). However, neutron-diffraction experiments on powder samples[27] and thin epitaxial films[28] showed that YH_3 has a HoD_3 structure, in which the H_{oct} atoms have shifted to positions in and close to the Y metal planes. Various total-energy calculations confirm that a shift of H_{oct} indeed lowers the total energy significantly.[32–34] Dekker *et al.* calculated a strongly increased electronic charge density for the HoD_3 structure in the plane containing the Y and H atoms compared to hcp.[32] Wang and Chou found additionally that the energy lowering by the H_{oct} displacement primarily comes from electron-ion interaction energy.[34] One thus can look at this as if the H_{oct} atoms are bound to the metal plane Y atoms forming a covalent binding, which explains the small (0.9%) a-axis expansion going from YH_2 to YH_3 (see Tables II and III). A strong repulsive interaction between nearest-neighbor H_{tet} pairs exists. In (hypothetical) hcp-YH_3 this repulsion is partially compensated for by the H atoms at the ideal octahedral positions, but in the HoD_3 structure this does not occur and there is a large c-axis expansion.[34]

For $0.38 < z < 0.67$ the volume expansion is smaller than 4%, and for $z < 0.38$ the lattice even contracts. This lattice contraction is caused by the interaction in the fcc structure between the RE metal d electron and the s electron of the octahedral H atom.[24] The measured lattice parameters for YH_3 agree within 1% with theoretical values[34] $a = 3.678$ Å and $c = 6.549$ Å.

Using the Scherrer equation[35] we determined the x-ray coherence length l_{coh} from the peak widths. We found $l_{coh} \sim 10$ nm, and that subsequent switching improves l_{coh}.

Although the Pd layer is only 15 nm thick, we observe in Fig. 3 the Pd (111) and (200) reflections at $2\theta = 40.12°$ and 46.66°, respectively [see Figs. 3(a) and 3(b)]. We determine for fcc Pd $a = 3.893 \pm 0.004$ Å , in agreement with the literature value[23] 3.8903 Å . The Pd peaks have shifted to 38.55° and 44.81° in Fig. 3(c), because of H absorption by the Pd, and we find $a = 4.045 \pm 0.004$ Å . Comparing this with bulk

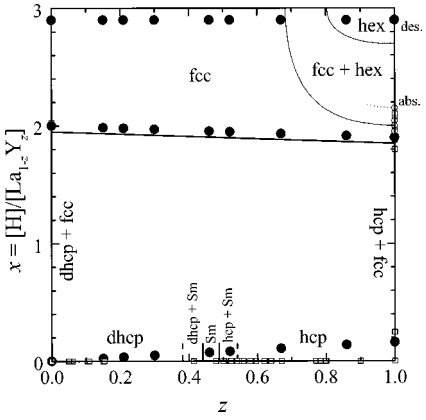

FIG. 6. Schematic composition diagram for $La_{1-z}Y_zH_x$ thin films at room temperature, based on our XRD measurements (solid circles). The hydrogen concentration x was derived as pointed out in the text. Thin lines indicate tentative phase boundaries for which no direct evidence is available yet. Small open squares are bulk data from literature (Ref. 17). Kooij *et al.* (Ref. 31) found a large difference in the YH_x thin-film phase diagram upon hydrogen absorption (abs.) and desorption (des.) for $2<x<3$ (open circles). The dotted line represents the $\beta+\gamma\rightarrow\gamma$ phase boundary for H-*absorption*.

values for the PdH_x system[36] gives $x=0.7$, as expected for a hydrogen pressure of 10^5 Pa at room temperature.

By combining our results combined with those from literature we construct the schematic phase diagram for the $La_{1-z}Y_zH_x$ system, as shown in Fig. 6. From XRD we conclude that the fcc-hcp phase boundary for $x=3$ lies at $z \leqslant 0.86$. However, the z dependence of the optical gap (see Sec. III E) suggests that this phase boundary is at $z \leqslant 0.81$.

In conclusion, thin polycrystalline $La_{1-z}Y_z$ alloys on quartz are *c*-axis oriented, and behave as the corresponding bulk alloys for $x=0$. No disproportionation takes place in the $La_{1-z}Y_zH_x$ system upon loading with hydrogen, and the preferential orientation is enhanced after the first loading. The latter two conclusions were confirmed by the dc resistivity measurements and the optical properties that are discussed below. Whereas all dihydrides are fcc, the trihydrides show a phase transition: for $z<0.67$ the films are fcc and for $z>0.81$ the films are hexagonal. The hexagonal trihydrides have an anomalously large c/a ratio, indicating another structure than hcp.

C. Pressure-composition isotherms

The pressure-composition $(p-x)$ isotherms as obtained from electrochemical H loading [see Eq. (4)] are shown in Fig. 7 for three alloys. Both La and $La_{0.45}Y_{0.55}$ are essentially hysteresis free, in agreement with optical measurements.[30] The YH_x isotherm exhibits large hysteresis, as discussed extensively by Kooij *et al.*[31] The latter isotherm shows a coexistence region during desorption, whereas the La-rich alloys exhibit no plateau, in agreement with XRD measurements. The shape of their isotherms indicates that these alloys remain fcc at all concentrations above $x=2$. There is no subplateau, related to the tetragonal phase that exists in bulk LaH_x at low temperatures.[17]

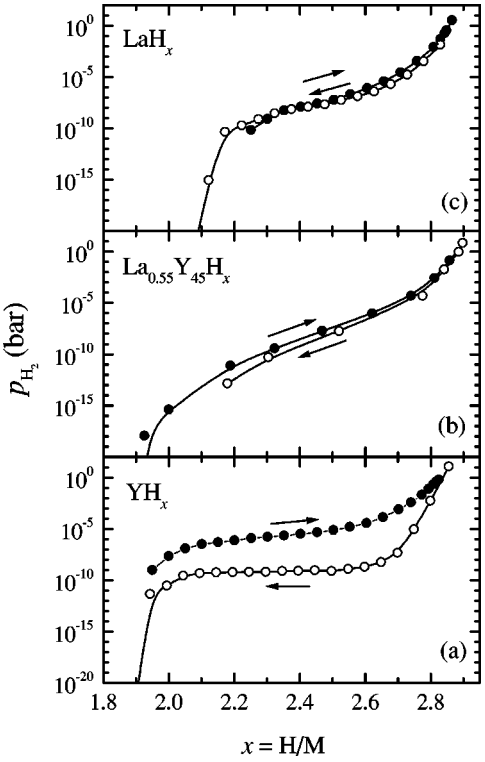

FIG. 7. Pressure-composition isotherms, determined electrochemically, for YH_x, LaH_x, and a $La_{0.55}Y_{0.45}H_x$ alloy at 295 K. The large hysteresis between ab- and desorption in YH_x as discussed by Kooij *et al.* (Ref. 31) is not present in the other two materials. This confirms the conclusion from Van Gogh *et al.* (Ref. 30) that the hysteresis is closely related to the fcc-hex structural phase transition.

We fitted the isotherms to Lacher's equation[37]

$$\ln p = 2\ln\left(\frac{x-x_1}{x_u-x}\right)+\frac{2}{kT}\left(E_0+E_{HH}\frac{x-x_1}{x_u-x_1}-\frac{E_b}{2}\right)+c(T), \tag{5}$$

and calculated the partial molar heat of solution ΔH for $La_{1-z}Y_zH_x$ via

$$\Delta H=\frac{F}{2}(E_{HH}+2E_0-E_b). \tag{6}$$

In Eq. (5) the hydrogen pressure p is in bar, x_u-x_l is the number of interstitial sites per metal atom, E_b is the H_2 binding energy (-4.46 eV), E_0 is the hydrogen energy, and E_{HH} is the H-H interaction energy. The term $c(T)=\frac{7}{2}\ln T - 7.051$ is material independent, and is equal to 12.85 for $T=295$ K. The results from the fits are given in Table IV.

The desorption ΔH values for LaH_x and YH_x agree within experimental accuracy with those for bulk material. The small E_{HH} values obtained for YH_x and LaH_x are consistent with the small lattice expansion during hydrogenation between $x=2$ and 3. The relatively large and positive E_{HH}

TABLE IV. Results of the fits of the isotherms in Fig. 7 to Lacher's equation [Eq. (5)] and the partial molar heat of solution calculated from Eq. (6).

z	x_l	x_u	E_0 (eV)	E_{HH} (eV)	ΔH (kJ/mole H)	ΔH_{lit} (Ref. 38) (kJ/mole H)
0	2.10	2.79	−2.64	0.05	−37.1	−42.0
0.46	1.98	2.90	−2.75	0.25	−38.1	−
1 (des)	1.97	2.71	−2.61	−0.10	−41.5	−44.9
1 (abs)	1.96	2.70	−2.54	−0.04	−31.8	−

for the alloy is, however, a clear indication of the existence of a wide distribution of site energies.[39,40]

D. Resistivity

1. dc resistivity for $x=0$ and 2

The z dependence of the dc resistivity ρ is given in Fig. 8 for the as-deposited $La_{1-z}Y_z$ films and the dihydrides $La_{1-z}Y_zH_2$. Open symbols are calculated from optical data (see below).

For both $x=0$ and 2 we observe a clear nonlinear behavior, which is well described by

$$\rho(z)=[\rho_{La}+(\rho_Y-\rho_{La})\times z]+4\rho_{do}\times z(z-1), \qquad (7)$$

with ρ_Y and ρ_{La} fixed. The constant ρ_{do} represents the effect of disorder scattering and is of the same order of magnitude

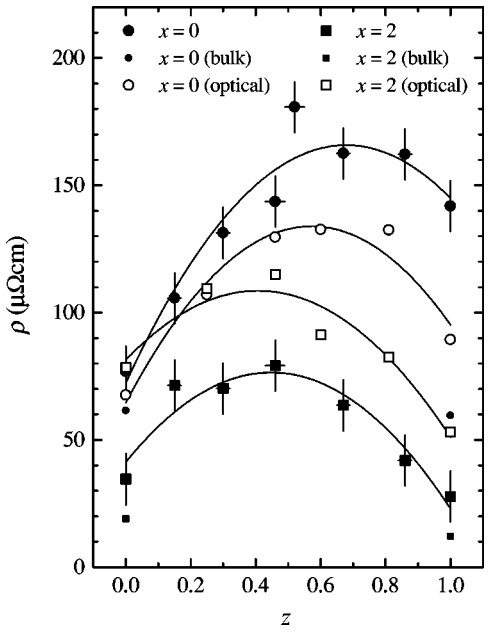

FIG. 8. Composition dependence of the dc resistivity of $La_{1-z}Y_zH_x$ (solid symbols). Small circles denote dc values of bulk La and Y (Ref. 23), and small squares of bulk LaH_2 and YH_2 (Ref. 17). Values calculated from optical measurements and Eq. (8) are indicated by open symbols. Solid lines are least-squares fits using Eq. (7). The large resistivity for as-deposited $La_{0.48}Y_{0.52}$ alloy is consistent with the fact that this film is in a Sm-hcp coexistence region (see Table I).

TABLE V. Drude Lorentz parameters for the as-deposited $La_{1-z}Y_z$ films. All parameters are in eV except ε_∞ and χ^2, which are dimensionless. In this work χ^2 is defined as the least-squares sum divided by two times the degrees of freedom.

z	0	0.25	0.46	0.60	0.81	1
ε_∞	0.461	0.117	2.435	1.515	0.423	1.823
ω_p	5.588	5.693	4.770	4.412	3.720	3.430
$1/\tau$	0.284	0.467	0.397	0.347	0.246	0.142
$\sqrt{f_1}$	8.065	11.216	6.334	1.294	3.259	4.090
ω_{01}	2.476	1.756	2.518	1.747	1.817	1.876
β_1	3.450	4.383	3.563	1.157	1.520	1.556
$\sqrt{f_2}$	6.299	2.193	6.559	9.836	8.477	7.324
ω_{02}	0.908	0.925	0.990	1.352	1.431	1.342
β_2	1.315	0.872	1.899	3.170	2.927	2.430
$\sqrt{f_3}$	3.675	2.784	3.441	5.016	6.471	7.248
ω_{03}	4.554	4.623	4.920	5.307	5.099	5.658
β_3	2.052	1.594	1.813	3.161	3.320	3.869
χ^2	0.057	0.050	0.049	0.033	0.053	0.065

as the resistivities of the parent metals (50 ± 10 $\mu\Omega$ cm and 45 ± 8 $\mu\Omega$ cm for $x=0$ and 2, respectively), indicating that conduction-electron scattering by impurities dominates electron-electron scattering and electron-phonon scattering. Two other observations validate this conclusion: (i) optical analyses (see Tables V and VI) gave relaxation times $\tau \sim 10^{-14}$ s, which means that electrons are scattered by phonons and/or impurities, but that electron-electron scattering is not important. (ii) The temperature dependence of the free-electron optical response showed a 20–30% increase of τ upon cooling from 300 to 4.2 K, indicating that defect

TABLE VI. Drude Lorentz parameters for $La_{1-z}Y_zH_x$ with $x=2$. All parameters are in eV except ε_∞ and χ^2, which are dimensionless.

z	0	0.25	0.46	0.60	0.81	1
ε_∞	2.460	0.575	0.802	0.735	1.407	2.198
ω_p	3.883	4.097	4.180	4.260	4.275	4.454
$1/\tau$	0.179	0.247	0.271	0.223	0.203	0.142
$\sqrt{f_1}$	1.497	1.765	1.831	1.873	1.935	2.001
ω_{01}	2.037	2.074	2.129	2.195	2.313	2.410
β_1	0.544	0.641	0.629	0.602	0.566	0.558
$\sqrt{f_2}$	3.641	3.946	3.914	4.011	3.958	4.039
ω_{02}	2.528	2.584	2.658	2.718	2.848	2.965
β_2	0.922	1.030	1.046	0.999	0.962	0.932
$\sqrt{f_3}$	7.335	9.341	9.283	9.383	7.864	7.633
ω_{03}	5.072	5.158	5.196	5.265	5.116	5.272
β_3	2.193	2.312	2.261	2.243	2.052	2.514
χ^2	0.129	0.130	0.145	0.170	0.238	0.242

scattering is comparable, though stronger than phonon scattering. The latter observation is consistent with the temperature dependence of ρ of 180 nm Y and YH_2 measured by Curzon and Singh.[41]

Note that the parabolic behavior is an indication of the high quality of our alloy films; oxidation, concentration inhomogeneities, and thickness variations readily blur disorder effects, causing much scatter in the measured values of ρ.

To obtain the electron mean free path $l_{\mathrm{mfp}}=v_F\tau$, the Fermi velocity v_F is estimated using $v_F=1/\hbar(\partial E/\partial k)_{k=k_F}$. From the band structure of La, calculated by Fleming *et al.*,[42] we find the largest Fermi velocity along AH with $v_F=7.9\times10^5\mathrm{ms}^{-1}$. For Y we expect larger values because of broader conduction bands. From the band structure calculations for Y of Altmann *et al.*[43] we find $v_F=9.9\times10^5$ ms^{-1} along LM. With $\tau=2.32\times10^{-15}$ s for La and $\tau=4.64\times10^{-15}$ s for Y (see Table V) we find $l_{\mathrm{mfp}}=1.8$ nm $(=4.9a)$ for La and $l_{\mathrm{mfp}}=4.6$ nm $(=13a)$ for Y.

For LaH_2 the calculations of Ng *et al.*[7] lead to $v_F=13.3\times10^5$ ms^{-1} along ΓX (see also Fig. 22). From the calculations for YH_2 of Peterman *et al.*[44] $v_F=9.6\times10^5$ ms^{-1} along ΓX. With $\tau=3.68\times10^{-15}$ s for LaH_2 and $\tau=4.64\times10^{-15}$ s for YH_2 (see Table VI) we obtain $l_{\mathrm{mfp}}=4.9$ nm $(=8.6a_{\mathrm{fcc}})$ for LaH_2 and $l_{\mathrm{mfp}}=4.5$ nm $(=8.6a_{\mathrm{fcc}})$ for YH_2.

Thus, both for the as-deposited films and the dihydrides $l_{\mathrm{mfp}}\sim10$ lattice spacings. This, together with the earlier conclusion that ρ is dominated by impurity scattering, implies that disorder is present on atomic length scales, i.e., Y and La atoms are mixed on an atomic length scale. That this holds both for $x=0$ and 2 is a further indication that the alloys are solid solutions and do not disproportionate upon hydrogenation.

The measured dc values for $x=0$ are larger than the literature values (see Fig. 8). Because at room temperature $l_{\mathrm{mfp}}\ll d$, with d the film thickness, the discrepancy cannot be a thin-film effect. We also rule out the presence of oxides in the film as a possible cause, because then the discrepancy should be larger for La, which is much more sensitive to oxidation. However, we did not observe this.

The thickness dependence of ρ for Y was studied by Curzon and Singh[41] for $20\leqslant d\leqslant200$ nm. They attributed the strong ρ increase for $d<90$ nm to oxide contamination. For $d>90$ nm oxide contamination no longer plays a role, as we already concluded above, and upon increasing d the resistivity decreases asymptotically to $\rho\approx120$ $\mu\Omega$ cm. This value is comparable to 144.9 $\mu\Omega$ cm found in this work. The fact that ρ does not decrease asymptotically to the bulk value means that surface effects are not important. Such effects are in general observed when $l_{\mathrm{mfp}}\sim d$, thus the measurements of Curzon and Singh imply that $l_{\mathrm{mfp}}\ll90$ nm that is consistent with $l_{\mathrm{mfp}}\lesssim10$ nm given above. Curzon and Singh attributed the discrepancy between bulk and thin films values above 90 nm to lattice defects: if films are well annealed, ρ turns out to decrease asymptotically to the bulk value.

A similar discrepancy exists between thin film and bulk values for the dihydride resistivities. Our value for YH_2 agrees perfectly with the 23 $\mu\Omega$ cm found by Curzon and Singh for a 180-nm YH_2 film.[41] We conclude that defect scattering accounts for the discrepancies for both $x=0$ and 2.

So far we have only discussed data obtained from resistivity measurements. Values for ρ can also be derived from optical measurements (described in Sec. II E) by means of the Drude equation

$$\rho_{\mathrm{opt}}=\frac{1}{\varepsilon_0\omega_p^2\tau}, \tag{8}$$

with ε_0 the vacuum permittivity, ω_p the plasma frequency and τ the electron relaxation time. Values for ρ_{opt} obtained from the parameters given in Tables V and VI are shown in Fig. 8. Although there is a difference in absolute values, ρ and ρ_{opt} exhibit the same trends, that is (i) the values for the dihydrides are smaller. For the La rich alloys this is not true for ρ_{opt}, but, because the difference in resistivities for $x=0$ and $x=2$ are much smaller than for Y-rich alloys, we attribute this to the fact that $\omega\tau\gtrsim1$, which means that intrinsic differences between ρ and ρ_{opt} may occur.[45] The low resistivities for YH_2 and LaH_2 are due to the larger v_{F} for $x=2$ compared to $x=0$. Tables V and VI show that it is a combined effect of larger values of ω_p and τ. (ii) The effect of disorder is reflected in both ρ_{dc} and ρ_{opt}. For $x=0$ we find $\rho_{\mathrm{do}}=52.5\pm7.5$ and 50.0 ± 1.0 $\mu\Omega$ cm for ρ_{opt} and ρ_{dc}, respectively. For $x=2$ we find $\rho_{\mathrm{do}}=40.0\pm7.5$ and 45.0 ± 7.5 $\mu\Omega$ cm for ρ_{opt} and ρ_{dc}, respectively. The effect of disorder is thus the same both at $\omega=0$ and optical frequencies $\omega\sim10^{16}$ s^{-1}.

In summary, for both $x=0$ and 2 the effect of disorder is of the same order of magnitude as the resistivity of the parent materials. Electron scattering is determined by defect scattering and $l_{\mathrm{mfp}}\sim10$ lattice spacings**,** which indicates microscopic mixing and no disproportionation. The scattering mechanisms are the same at optical frequencies as for the dc case.

2. dc resistivity for $2<x<3$

Figure 9 shows the concentration dependence of the resistivity together with its time derivative during the second hydrogenation from the dihydride to the trihydride. The behavior is representative for subsequent loading cycles. The final resistivities are of the order of 1 mΩ cm. These low values are caused by shunting of the active layer by the metallic Pd cap layer when the resistivity of the $La_{1-z}Y_zH_x$ becomes very large. One can correct for the Pd layer by treating the $La_{1-z}Y_zH_x$ and Pd layer as two parallel resistors with resistance R and R_{Pd}, respectively. The measured resistance is then $R_{\mathrm{tot}}=R_{\mathrm{Pd}}R/(R_{\mathrm{Pd}}+R)$ and the corrected resistivity

$$\rho_{\mathrm{corr}}=\frac{\rho\rho_{\mathrm{PdH}_x}d}{\rho_{\mathrm{PdH}_x}d_{\mathrm{tot}}-\rho d_{\mathrm{PdH}_x}}, \tag{9}$$

with d_{tot} the sum of the thickness d_{PdH_x} of the cap layer and the thickness d of the active layer. With $\rho_{\mathrm{PdH}_x}=0.1$ mΩ cm, we find for all alloys $\rho\sim100$ mΩ cm, which is three orders of magnitude larger than for $x=0$.

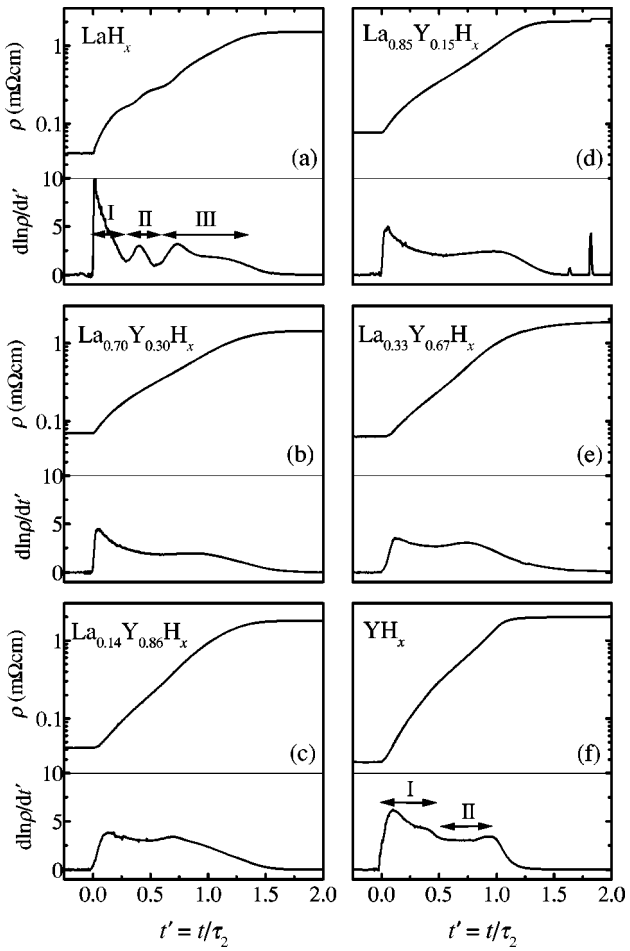

FIG. 9. Time dependence of the resistivity of six $La_{1-z}Y_zH_x$ alloys during the second absorption from the dihydride to the trihydride. To compare the curves, the time was scaled by the switching time τ_2 as defined in Sec. III A. The time derivative clearly exhibits various loading stages. In (d) the hydrogen pressure was increased at $t'=1.6$ and 1.8, causing peaks in the time-derivative of ρ.

The time derivatives in Fig. 9 indicate several reproducible stages during hydrogen absorption. All films, except LaH_x, exhibit a two-stage absorption. After an initial steep increase of ρ a tendency to saturation occurs near $t'\approx 0.5$, after which ρ increases faster again. LaH_x shows even a three stage absorption. The increase of ρ in stages does not seem to be caused by a structural phase transition of the metal atoms; for $0.30\leqslant z\leqslant 0.67$ a similar behavior is observed as for $z\geqslant 0.86$, whereas in the latter region the films exhibit an fcc-hex phase transition. However, the different stages might be caused by hydrogen ordering. For $2<x<3$ phases are known to exist in which the randomly distributed hydrogen vacancies order in planes.[17] Such transitions are likely to affect the resistivity.

We observed that the loading speed for $p_{H_2}\lesssim 1$ bar is linearly proportional to the hydrogen pressure both in the α phase as for $x>2$. The linearity indicates that the switching kinetics are controlled either by H_2 transport in the gas phase or by H_2 dissociation.[46] Note that this confirms our assumption that the loading pressures are low enough to ensure quasiequilibrium.

We have used the above result to scale the switching times to values expected for 1000-mbar H_2. In this way we are able to compare the switching times. No significant z-dependence of the switching times is observed. For the first loading we find $\tau_1=20\pm 13$ s. During the second loading the films switch roughly five times faster than for the first loading, and we find $\tau_2=4.0\pm 1.8$ s, in agreement with values of van der Molen *et al.*[47] Subsequent loadings behave like the second loading. The ''virgin'' effects are likely to be caused by the irreversible α-β transition that occurs for all films during the first loading, in which the films transform from an hexagonal structure (hcp, dhcp, or Sm) into an fcc structure. Another virgin effect is caused by the Pd cap layer. During the first loading the wetting of the cap layer is improved by the large heat of formation of the $(RH)H_x$ and the PdH_x. A better wetting causes the film to be faster during subsequent loadings. This is consistent with our observation that the resistivity of the trihydride is significantly lower after the second loading for films covered with only 5 nm Pd. During the first loading the initial Pd islands transform into a closed layer that shunts efficiently the highly resistive trihydride.

From this section we conclude that switching times decrease with a factor 5 after the first loading. Intrinsic resistivities of trihydrides (i.e., corrected for the Pd cap layer) are ~ 100 mΩ cm. Hydrogenation in three stages is observed for LaH_x for $2<x<3$, whereas all other films exhibit a two stage hydrogenation. The stages might be due to ordering of H vacancies.

E. Optical properties

1. Optical properties for $x=0$

Even more remarkable than the electric properties are the optical properties of switchable mirrors, since their MI transition is accompanied by dramatic changes in the reflectance and transmittance in the visible part of the spectrum. In this section we present what we believe is the first detailed investigation of the dielectric function $\varepsilon(\omega)$ of $La_{1-z}Y_zH_x$. The dielectric function $\varepsilon(\omega)$ of the as-deposited $La_{1-z}Y_z$ alloys, obtained from ellipsometry after correction for the substrate and the Pd layer, is shown in Fig. 10. Few data for either Y or La exist in the literature. One reason for this is their sensitivity to oxidation, which can severely affect the reflectivity. However, accurate measurements on single crystalline bulk samples of Y over a wide range of energy and temperature were done by Weaver and co-workers[48,49] who measured reflectivity with the electric field vector perpendicular ($\perp$) and parallel ($\parallel$) to the c axis, and determined $\varepsilon(\omega)$ by a Kramers-Kronig analysis. Below 4 eV a strong anisotropy is observed. For polycrystalline samples $\varepsilon_{\rm poly}(\omega)=\frac{1}{3}\varepsilon_{\parallel}(\omega)+\frac{2}{3}\varepsilon_{\perp}(\omega)$ would be expected. However, our $\varepsilon(\omega)$ is similar to $\varepsilon_{\perp}(\omega)$ of Weaver and co-workers. We do not see any contribution of $\varepsilon_{\parallel}(\omega)$, which should be readily visible due to the large difference between $\varepsilon_{\parallel}(\omega)$ and $\varepsilon_{\perp}(\omega)$ for energies below 4.5 eV. We therefore conclude that, although polycrystalline, our films are preferentially orientated with the c axis perpendicular to the substrate. This is consistent with the XRD measurements (see Sec. III B).

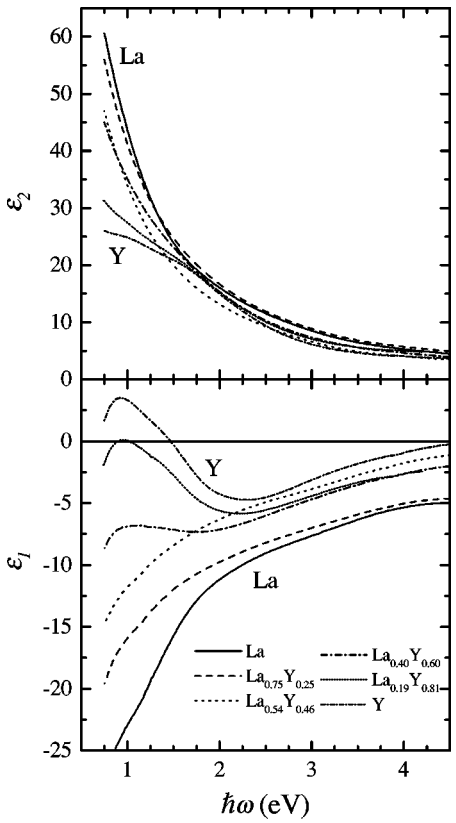

FIG. 10. Real and imaginary part of $\varepsilon(\omega)$ of the as-deposited $La_{1-z}Y_z$ films, as determined from ellipsometry.

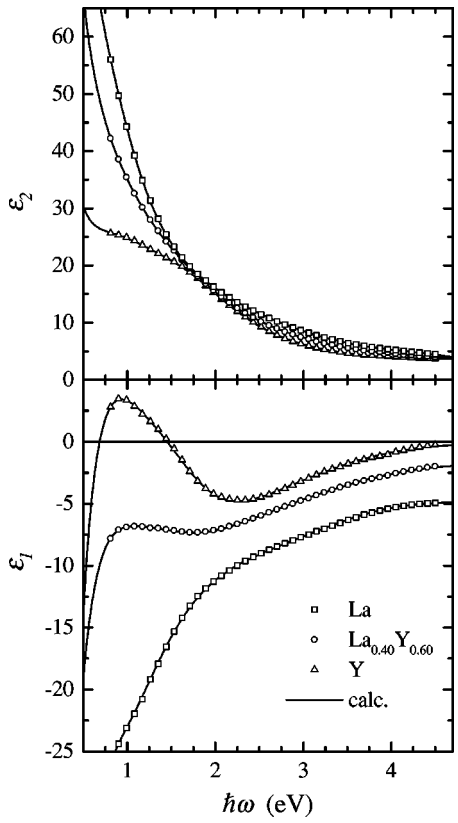

FIG. 11. Results of the fits of $\varepsilon(\omega)$ using the DL parametrization [Eq. (10)] for La, Y and a $La_{0.40}Y_{0.60}$ alloy. Symbols represent measured values and the solid line is the result of the fit (see Table V). For clarity, results are shown for three representative materials only and not all experimental data points are shown.

To analyze the data quantitatively, we model $\varepsilon(\omega)$ using a sum of one Drude oscillator and three Lorentz oscillators (LO's):

$$\varepsilon(\omega)=\varepsilon_1+i\varepsilon_2=\varepsilon_\infty-\frac{\omega_p^2}{\omega^2+i\omega/\tau}+\sum_{j=1}^{3}\frac{f_j}{\omega_{0j}^2-\omega^2+i\omega\beta_j}. \tag{10}$$

The constant ε_∞ in Eq. (10) accounts for excitations far above 4.5 eV. The second term describes the free-carrier response and is of Drude form, characterized by the plasma frequency ω_p and the relaxation time τ. The last three terms represent the effect of interband and/or impurity absorptions. Each LO is characterized by an oscillator strength *f*, a resonance frequency ω_0 and a broadening parameter β. The choice for *three* LO's is supported by fit results using two and four LO's; it turns out that two LO's clearly give worse fits than three LO's, whereas fitting four LO's leads to zero strength of the fourth LO. The excellent quality of the fits obtained by means of Eq. (10) is demonstrated for three materials in Fig. 11. Similarly, good fits are obtained for all alloys as can be seen from the χ^2 values in Table V.

Modeling the optical properties with a Drude-Lorentz (DL) parametrization has several advantages: (i) It often gives a good description of both metals and insulators, and is therefore particularly suitable to study the MI transition in RE hydrides. (ii) Contrary to some other parametrization models, its parameters have a physical meaning. (iii) The model is intrinsically Kramers-Kronig consistent, and therefore implicitly checks the reliability of the experimental data. (iv) Often $\varepsilon_2(\omega)$ is calculated from the one-electron band structure by a calculation of the joint density of states (JDOS) and dipole transition matrix elements. Many-particle effects are not included, and therefore it is impossible to obtain the free-electron contribution to $\varepsilon_2(\omega)$ from such a calculation. For a good comparison with experiment and (one-electron) theory, one thus needs a way to separate the interband absorption contribution from the free-electron contribution, for which Eq. 10 is particularly useful.

The data in Table V show that large interband absorptions, centered at ω_{01} and ω_{02}, occur below the plasma frequency ω_p, which is typical for transition metals. The structures in $\varepsilon_2(\omega)$ are estimated at 1.1 and 1.7 eV from Fig. 10, and are comparable with the bulk values[49] 1.15 and 1.75 eV.

The interpretation of the optical results is hindered by the fact that only few band-structure calculations exist for Y and La for the correct lattice structures. Calculations of the JDOS do not exist at all to our knowledge. However, the band structure and density-of-states (DOS) calculations of Altmann and Bradley[43] provided some information. Their DOS, which corresponds well to photoemission data,[50] and their band structure suggest that the broad structure extending from $\lesssim$0.75 to 2.5 eV originates from interband absorptions between *d* bands along Σ and T'. However, the width of the

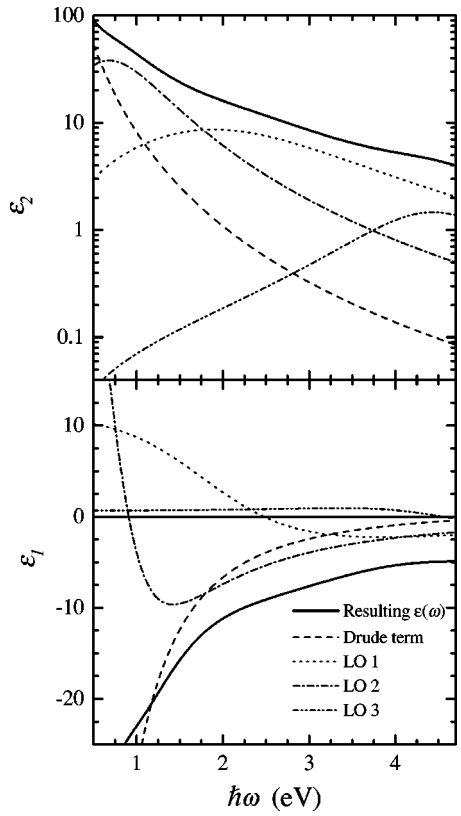

FIG. 12. $\varepsilon_1(\omega)$ and $\varepsilon_2(\omega)$ of lanthanum decomposed in a Drude contribution and three Lorentz oscillator contributions according to Eq. (10).

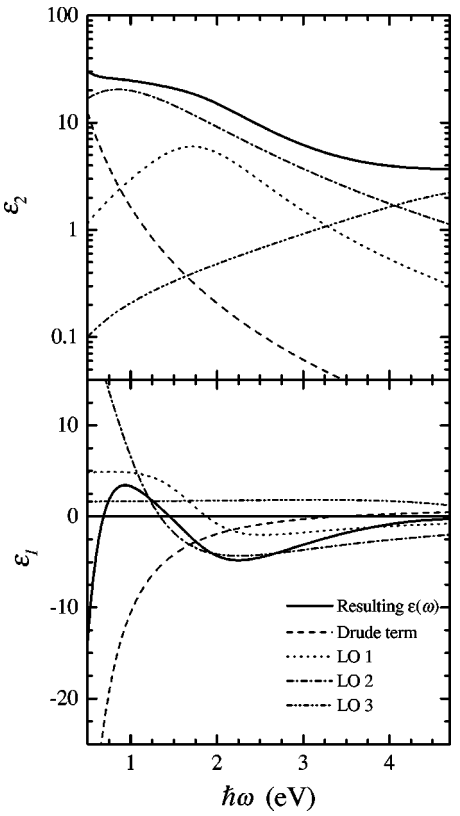

FIG. 13. As Fig. 12, but now for the Y case.

experimental absorptions and the lack of calculations of the JDOS and dipole transitions matrix elements make it extremely difficult to identify the origin of interband absorptions unambiguously.

Figure 10 suggests that the electronic structure of La and Y differ very much. However, after a decomposition of $\varepsilon(\omega)$ into free- and bound-electron contributions, as shown in Figs. 12 and 13, it is clear that the interband absorption properties are actually very similar. The difference in their $\varepsilon(\omega)$ is only caused by the interplay of the Drude and contribution of the first LO. Both contributions are large and have opposite signs in $\varepsilon_1(\omega)$. Therefore relatively small differences in the DL parameters result in large differences in the resulting $\varepsilon(\omega)$.

The z dependences of the various DL parameters exhibit some clear trends. First, the plasma frequency decreases linearly with z, which is opposite to what one would naively expect from the larger volume of La, as ω_{p} is proportional to the free-electron density. However, the intrinsic free-electron properties, which in the simple Drude model are represented by ω_p, depend strongly on the band structure near the Fermi energy, which is markedly different for La and y. Second, we see a clear nonlinear behavior of the relaxation time. This is due to disorder, and related to the nonlinear behavior of the resistivity shown in Fig. 8.

Third, the interband absorptions shift monotonically to the blue upon increasing z. This observation is not immediately clear for ω_{01} in Table V. The reason for this is that for decreasing z the widths of the two interband features at ω_{01} and ω_{02} increase, and their maxima tend to merge. As a result the parameters of the first two LO's become strongly coupled, and clear trends for the parameters of the two separate LO's disappear. For $z \lesssim 0.50$ it would have been more physical to use only one LO for the interband absorption feature around 1.5 eV. Hence, for a meaningful physical interpretation the first and second LO's should be treated as one interband feature. This feature exhibits a clear red shift upon decreasing z, which points to a narrowing of the bands, caused by the 14% larger volume of La compared to Y. The volume effect is much stronger than the broadening effect due to larger radii of $4sp5d$ orbitals of La compared to the $3sp4d$ orbitals of Y. We will see the same effect in the dihydrides discussed below.

The measured optical properties indicate that the alloy is not a mesoscopic mixture of Y and La, in correspondence with the XRD results. We find for each alloy that $\varepsilon(\omega)$ is not enclosed over the whole spectral range by the corresponding Wiener bounds.[51,52]

We conclude that the optical properties of $La_{1-z}Y_z$ alloys are well described by a DL model. All alloys show interband absorptions below the plasma frequency, and these interband absorptions shift to higher energies on increasing z. Clear disorder effects are observed in the optical properties.

2. Optical properties for $x=2$

The dielectric functions for the $La_{1-z}Y_zH_2$ (dihydride) films, obtained from ellipsometry after correction for the

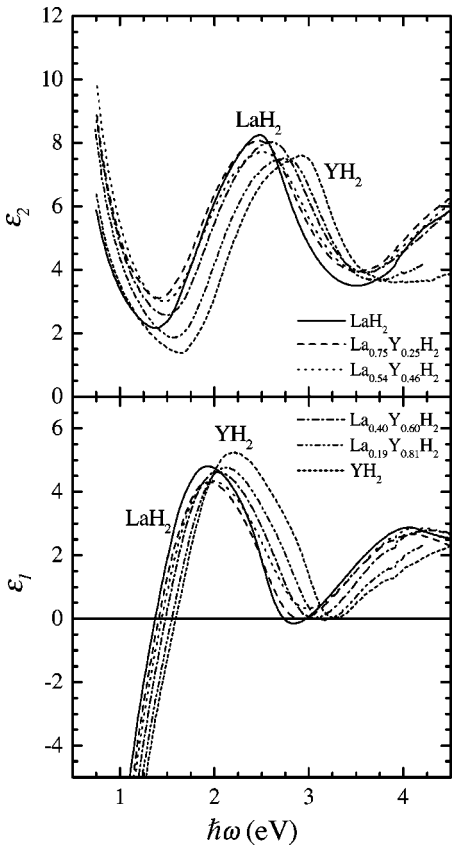

FIG. 14. Imaginary and real part of the dielectric functions for the $La_{1-z}Y_zH_2$ dihydride films, obtained from ellipsometry.

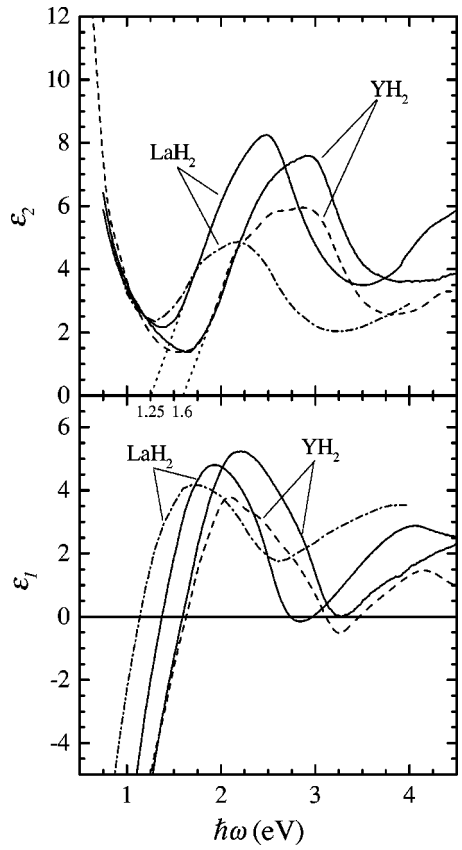

FIG. 15. Comparison of $\varepsilon(\omega)$ of YH_2 and LaH_2 measured on thin films by means of ellipsometry (solid lines) with literature values obtained from absorption measurements on bulk samples (Weaver *et al.* (Ref. 19) dashed lines; Peterman *et al.* (Ref. 54), dash-dotted line). Interband absorption onset energies of LaH_2 and YH_2 were estimated by extrapolating ε_2 to zero.

substrate and the Pd layer, are given in Fig. 14. For all alloys interband absorptions exist below the plasma energy, which is typically 4 eV. At low energy a free-electron behavior is discerned and around 2.5 eV interband absorptions are visible. Around 4.0 eV there is an onset to another interband absorption band, that extends outside the measuring range. As in the $x=0$ case, typical features shift to higher energies on increasing z.

The optical properties of YH_2 are well understood, since the thorough studies of Weaver and co-workers[19,53] and Peterman and co-workers[44,54] Calculations of the electronic structure were shown to agree quantitatively with optics and photoelectron spectra. The structure in ε_2 around 2.5 eV (see Fig. 14) is caused by interband absorptions within the *d*-like complex of bands along Q, W-K, and Σ in the first Brillouin zone of the fcc lattice (see Sec. III E 4). The interband absorption onset increases along the sequence ScH_2(1.25 eV) $\rightarrow YH_2$(1.6 eV)$\rightarrow LuH_2$(1.9 eV) as a result of *d*-band dilation along $3d\rightarrow 4d\rightarrow 5d$.[53] In this light, the 1.3-eV onset for LaH_2 seems anomalous. However, the *d* bands of LaH_2 are strongly narrowed due to its large atomic volume (31% larger than for YH_2 and 45% larger than LuH_2), which surpasses the *d*-band dilation.[54] From calculated band structures for YH_2 and LaH_2 we find for the onset for interband transitions 2.1 and 1.3 eV, i.e., a difference of 0.8 eV.[7,44] From Fig. 15 and our DL fits (see Table VI), we estimate 0.4 eV, which is a reasonable agreement. Narrowing of the *d* bands also lowers the spectral width of the interband absorption feature in ε. From our measurements we estimate a difference of 0.3 eV.

Another indication that the interband absorptions arise from transitions between *d* bands is that the difference in interband onset between LaH_2 and LuH_2 can be understood as a pure volume effect, because both materials have $5d$ valence. For *d* states the bandwidth scales as a^{-5}, with a the lattice spacing.[55] The ratio of the interband onset energy $E^{\text{onset}}_{\text{LaH}_2}$ for LaH_2 and $E^{\text{onset}}_{\text{LuH}_2}$ for LuH_2 is thus given by

$$\left(\frac{E^{\text{onset}}_{\text{LaH}_2}}{E^{\text{onset}}_{\text{LuH}_2}}\right)=\left(\frac{a_{\text{LuH}_2}}{a_{\text{LaH}_2}}\right)^5. \tag{11}$$

With $E^{\text{onset}}_{\text{LuH}_2}=1.9$ eV,[19] $E^{\text{onset}}_{\text{LaH}_2}=1.2$ eV, $a_{\text{LuH}_2}=5.033$ Å,[36] and $a_{\text{LaH}_2}=5.694$ Å (see Table II), we find 0.63 and 0.54 for the left- and right-hand sides, respectively, which is a reasonable agreement.

Absorption above 3.5 eV arises from interband transitions mainly between the parallel bands along Σ, where the lower band is *d*-*s* like and the upper band is *d* like.[53] The sharp

structure in ε_2 around 5 eV, from which in Fig. 14 only the onset is visible, is due to the flatness of the lower *d*-*p* band near the K point.

Figure 15 shows that there is qualitative agreement between our results for YH_2 with those measured on polycrystalline bulk samples.[19] Our maximum values of ε_1 and ε_2 are somewhat higher, and instead of three interband features between 2 and 3 eV we observe only two. We also do not observe the decrease of ε_1 at 4.3 eV. However, the energies of different features in both YH_2 spectra are the same. The bulk values were obtained by a Kramers-Kronig (KK) analysis of absorption spectra. For such an analysis one needs to extrapolate the absorption both to zero and infinite energies, and it is well known that this can introduce inaccuracies in the final result for $\varepsilon(\omega)$. In our case, however, $\varepsilon(\omega)$ is obtained essentially directly. We believe that the differences of our results with those on bulk YH_2 are thus related to this KK transformation and are not a thin film effect.

There is a larger disagreement between our results for LaH_2 and the results obtained for bulk material, both in magnitude and in the energy positions of typical features. We have some indications that our measurements are more accurate than the bulk values: (i) The oxidation behavior of LaH_x is notorious, and it is well known that a surface oxide can affect severely the reflectivity of a material. Our technique, where we measure through the substrate, seals well the LaH_x from the ambient. (ii) The reflectance-transmittance spectra, calculated from our $\varepsilon(\omega)$, are in excellent agreement with direct reflectance measurements. This is not possible with the bulk dielectric function. In particular, the good agreement for the measured transmittance indicates that our $\varepsilon(\omega)$ is not affected by surface artifacts, since the transmittance probes the optical properties throughout the film and is rather insensitive to surface effects. (iii) In sharp contrast to our thin film data and the bulk YH_2 data, we cannot obtain a good DL fit of the bulk LaH_2 data. (iv) Our experimental interband absorption onset energy agrees very well with the theoretical value.

In addition to the XRD results, the optical properties of the dihydride films indicate that the alloys do not disproportionate upon hydrogenation. We find for each alloy that $\varepsilon(\omega)$ does not fall between its Wiener bounds[51] over the whole spectral range, which indicates that the alloys are not mesoscopic mixtures of YH_2 and LaH_2.

To analyze the optical properties of the dihydride alloys, we again use a DL parametrization for $\varepsilon(\omega)$. The results are listed in Table VI. Although the values of χ^2 are somewhat larger than in the $x=0$ case, we still obtain good fits (see Fig. 16). The DL description of $\varepsilon(\omega)$ uses rather simple functional forms to model $\varepsilon(\omega)$ that is the result of a complicated electronic structure. Therefore, χ^2 is expected to be larger when structures in $\varepsilon(\omega)$ are more pronounced. This is what is the case here; the larger χ^2 for $x=2$ compared to the $x=0$ case is mainly due to the misfit for $1.25 \leqslant \hbar\omega \leqslant 2$ eV. As for $x=0$, adding another LO does not improve the fit.

In summary, the DL model describes well the optical properties of the dihydrides. Interband features appear at higher energies for larger *z*, and effects of disorder are observed in the optical properties of the dihydrides.

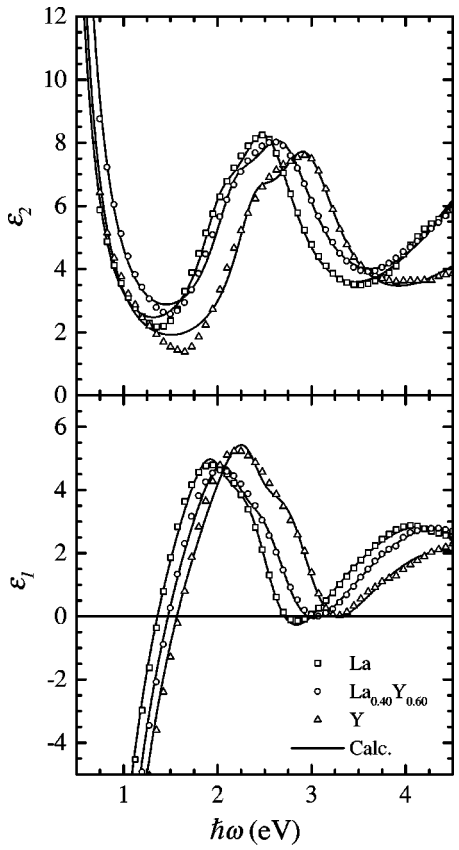

FIG. 16. Fits of the $\varepsilon(\omega)$ measured with ellipsometry for LaH_2, $La_{0.40}Y_{0.60}H_2$, and YH_2. For clarity, results are shown for only three alloys, and not all data points are plotted.

3. Dihydride transmittance window

A peculiar optical property of YH_2 is that, although the material is a low-resistivity metal, it is slightly transparent in the red part of the optical spectrum. This window arises from a combination of small free-electron absorption, because the photon energies are close to the (screened) plasma energy, and low interband absorption. This results in a narrow region where the total absorption is small, and therefore the film is transparent even for rather thick films. Such transmission windows are present at higher energies in Au, Cu, and Ag. Based on the similar shape of $\varepsilon(\omega)$ for all $La_{1-z}Y_zH_2$ such a dihydride transmission window is expected to exist in all alloys. For this we measured directly the optical transmittance and reflectance of the dihydrides for different alloys. The transmittances are shown in Fig. 17.

Figure 18(a) shows that there is a monotonic shift of $\hbar\omega_{\max}$ going from 1.52 eV for LaH_2 to 1.78 eV for YH_2. However, the amplitude is suppressed upon alloying in a very nonlinear fashion [see Fig. 18(b)]. The amplitude is minimal for $z=0.46$, and is one order of magnitude lower than for YH_2 or LaH_2. This suggests that the strong suppression is related to disorder. From a close analysis of the DL parameters in Table VI we find that disorder effects enter Eq. (10) via the DL parameters ε_∞, the resonance frequencies ω_{0i}, and the broadening parameters β of the second and third LO, and τ.

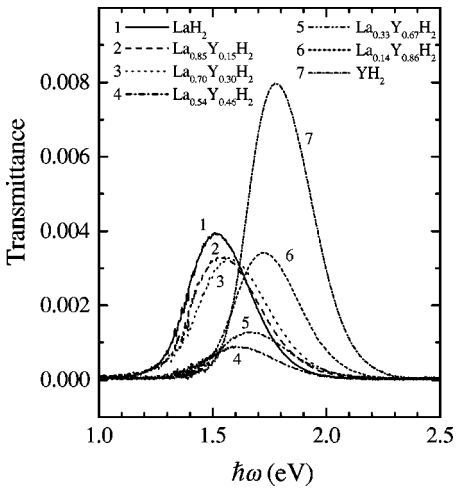

FIG. 17. Dihydride tranmission windows for the $La_{1-z}Y_zH_2$ alloys. Although the transmission window is observed for all alloys, its magnitude is strongly suppressed upon alloying.

To explore the role of disorder, we calculated the transmittances of a 15-nm Pd/300-nm $La_{1-z}Y_zH_x$/Suprasil stack with a DL parametrization of $\varepsilon(\omega)$, with all parameters linearized. Then we took the fitted values for one parameter and again calculated the dihydride windows, and so on. The dihydride window is 40% reduced by the nonlinearity of ε_∞, and 15% by the nonlinearity of each of the parameters τ, ω_{0i}, and β_i. We conclude that the strong suppression of the dihydride window is caused by disorder, the largest contribution coming from optical absorptions at energies much larger than 4.5 eV.

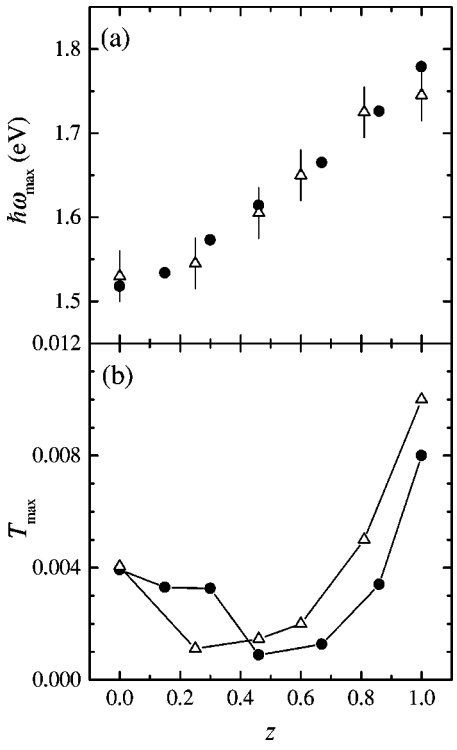

FIG. 18. Alloy concentration dependence of the position $\hbar\omega_{\max}$ and amplitude $T_{\max}$ of the dihydride transmission window in $La_{1-z}Y_zH_x$ (see Table VI). The solid circles are from direct transmittance measurements. The open triangles were calculated using the measured $\varepsilon(\omega)$.

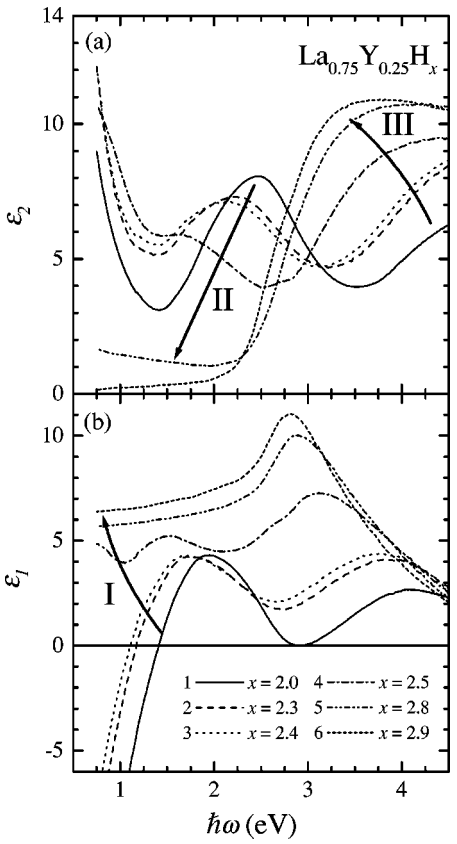

FIG. 19. Hydrogen concentration dependence of $\varepsilon(\omega)$ for $La_{0.75}Y_{0.25}H_x$ upon hydrogenation from the dihydride. This film contracts and stays fcc when x increases from 2 to 3 (see Fig. 4).

4. Optical properties for $2<x<3$

The variation of $\varepsilon(\omega)$ upon hydrogenation from $x=2$ for two alloys and YH_x is given in Figs. 19, 20, and 21. The qualitative behavior of all alloys is similar. The main trends indicated by arrows in these figures are (I) the disappearance of the free electron optical response with increasing x, (II) a suppression of the interband absorptions around 2.5 eV, and (III) a shift to lower energies of the second interband absorption peak in ε_2. We can immediately conclude that the systematic lowering in energy of the interband transitions is *not* caused by volume changes as LaH_x contracts for $x=2\rightarrow3$, $La_{0.54}Y_{0.46}H_x$ expands slightly, and YH_x expands a great deal. The origin of the trends can, however, be understood from the band structures for LaH_2 and LaH_3 calculated by Ng *et al.*[7] (see Fig. 22).

In their calculations, the insulating nature of LaH_3 is due to electron correlations at the hydrogen sites, which narrows the valence band with strong hydrogen 1*s* character, and causes a gap to open. From a comparison of the band structures of LaH_2 and LaH_3 [Figs. 22(a) and 22(b), respectively] we see that LaH_3 differs from LaH_2 in a newly formed band below the Fermi energy. The rest of the band structure re-

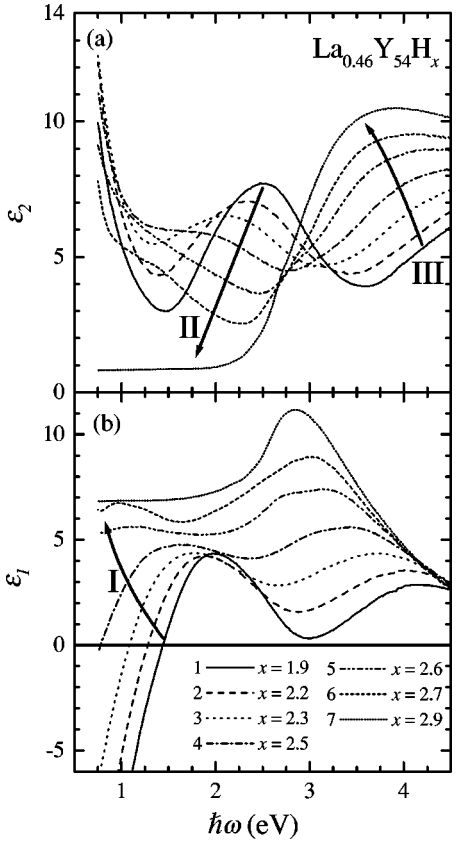

FIG. 20. Hydrogen concentration dependence of $\varepsilon(\omega)$ for $La_{0.46}Y_{0.54}H_x$ upon hydrogenation from the dihydride. This film slightly expands when x increases from 2 to 3, but it stays fcc.

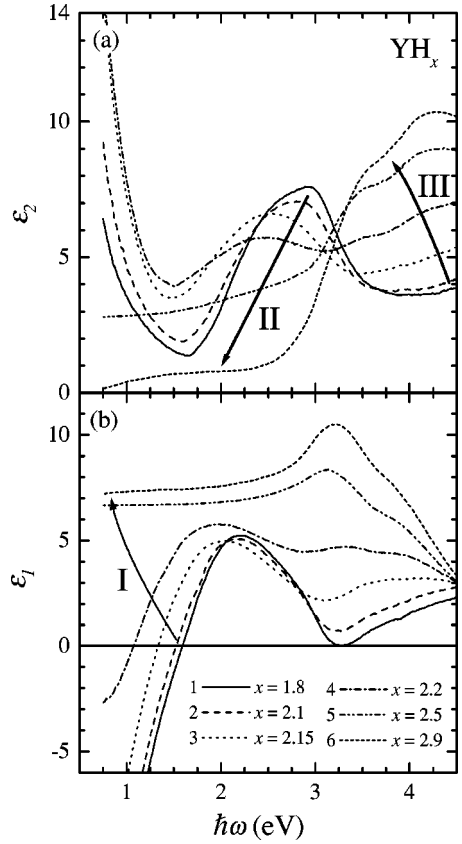

FIG. 21. Hydrogen concentration dependence of $\varepsilon(\omega)$ for YH_x. Although YH_x transforms from fcc to hex going from $x=2$ to 3, accompanied by a large, uniaxial expansion, the qualitative behavior of the optical spectra is the same as for the $La_{1-z}Y_zH_x$ alloys in Figs. 19 and 20.

mains essentially unaffected. Hybridization occurs along Δ, and pushes bands 1 and 2 away. Furthermore, small effects near W and K are observed. Along Λ and Σ a new band appears as a flat band above band 2. Near x the new band has pushed band 3 upward above band 4. Along Q and Σ, band 3 is also pushed upward above E_F.

We now discuss the three trends mentioned above.[56] First, the decrease of the plasma frequency is consistent with the Kondo insulator picture of Ng *et al.* Above $x=2$ every additional hydrogen binds an electron of the host metal into a sort of inert Zhang-Rice singlet. This leads to a linear depletion of the free-electron density. In a band picture this would correspond to a gradual shift of spectral weight from band 3 in LaH_2 to band 3 in LaH_3.

Second, we consider the weakening and shift downward in energy of the interband absorptions around 2.5 eV. We saw before that they arise from transitions between the d bands 3 and 4 along Q, W-K, and Σ. By adding hydrogen, the states of band 3 hybridize to much lower energies, and as a result the optical interband transitions lose strength and finally disappear. Adding hydrogen causes more and more disorder. This can lead to band flattening, and consequently to a red shift of the interband absorptions.

The third effect is that interband absorptions present in the dihydride at high energies (>3.5 eV) also shift toward lower energy upon increasing x. Note that the onset of these transitions determine the final appearance of the thin-film transparent state: LaH_3 is orange and YH_3 is yellow. We saw earlier that high-energy absorption in the dihydride is caused by transitions between bands 2 and 3 along Σ. Figure 22 suggests that the energy shift is merely a combination of the disappearance of these initial transitions by hybridization of band 3 with the hydrogen 1s states and the appearance of transitions between the newly formed s band and band 4 near Γ [see Fig. 22 (b)]. Although a neat calculation of ε_2 should be made to conclude on this, Figs. 19 and 20 suggest that the increased strength of the high-energy interband transitions originates from the flatness of the new band near Γ. Note that the band-gap in Fig. 22(b) is 2 eV, in good agreement with the experimental value of 1.9 eV.

In conclusion, the qualitative behavior of the optical properties of $La_{1-z}Y_zH_x$ alloys between $x=2$ and 3 is the same for all z. This again shows the robustness of the MI transition and its independence on the lattice structure. The MI transition in films that remain fcc indicates that the phase transition is not a discontinuous transition, but merely a continuous decrease of conduction electrons.

5. Optical properties for $x=3-\delta$

In Fig. 23 dielectric functions are shown for the alloys in their insulating trihydride state. The dielectric functions in

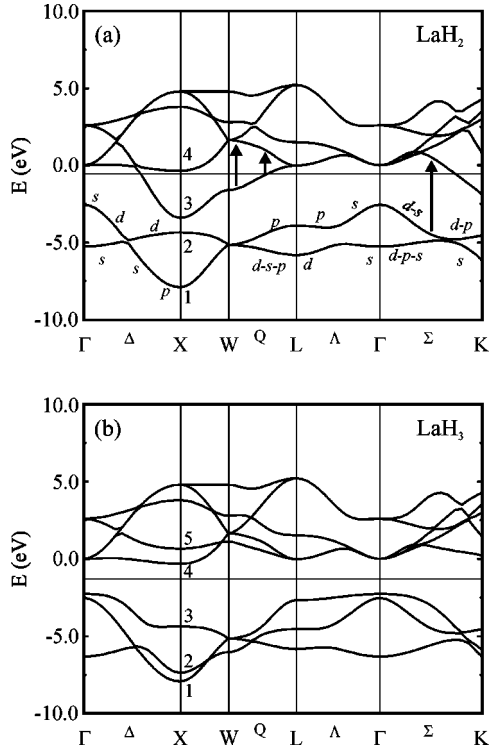

FIG. 22. Band structures for LaH_2 and LaH_3 (both fcc) calculated by Ng *et al.* (Ref. 7) The character of the bands below E_F (indicated in decreasing magnitude) were calculated by Weaver *et al.* for the similar YH_2 (Ref. 53). The bands above E_F have mainly *d* character. Arrows in (a) indicate positions in reciprocal space where strong optical absorption occurs: transitions along *Q* contribute to the structure in ε_2 around 2.5 eV (see Fig. 14), and transitions along Σ are mainly responsible for the structure at $\hbar\omega \gtrsim 4$ eV.

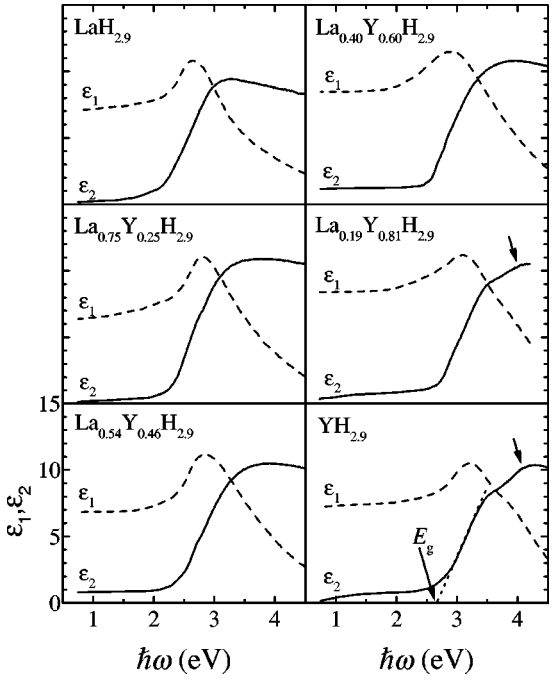

FIG. 23. Dielectric functions measured with ellipsometry for the alloys $La_{1-z}Y_zH_3$ in their insulating trihydride state. The optical band gap E_g was estimated by extrapolating ε_2 to zero. For $z = 0.81$ and 1, an extra absorption is observed around 4.2 eV, indicated by a short arrow.

Fig. 23 are typical for insulators. When the energy approaches the band gap energy from below, ε_2 increases strongly because absorption starts. For $z = 0.81$ and 1 an extra absorption above the optical gap exists near 4.2 eV (see Fig. 23). Apparently this is characteristic for hexagonal trihydrides.

Figure 23 shows that $\varepsilon_2(\omega)$ is not completely zero below the optical gap. Depending on *z*, absorption below the optical gap extends to 1–1.8 eV below the optical gap. This effect is also observed in the transmittances of the $La_{1-z}Y_zH_3$ films (see Fig. 24). The transmittance below the optical gap becomes significantly smaller when $z \rightarrow 0.5$, which points to a disorder effect. The absorption below the optical gap might be due to lattice defects. It is also conceivable that because of disorder dipole forbidden transitions become allowed. This would be in agreement with *GW* calculations of van Gelderen *et al.*[11] that predict a fundamental gap that is dipole forbidden. The inset of Fig. 24 shows that the maximum achievable transmittance lies between 65% for a $La_{0.85}Y_{0.15}H_3$ alloy and only 15% for a $La_{0.33}Y_{0.67}H_3$ alloy.

In addition to ellipsometric data we also analyzed transmittance spectra of the trihydride alloys shown in Fig. 24 to estimate the optical gap E_g. For this we first determined the frequency dependent absorption coefficient using the Lambert-Beer law

$$T(\omega) = T_0 \exp[-\alpha(\omega) d], \tag{12}$$

with *d* the film thickness of the $La_{1-z}Y_z$ layer, and T_0 containing the absorptions of the other layers and the reflections at all interfaces. By assuming parabolic bands, the following forms for $\alpha(\omega)$ near the optical gap can be derived from time dependent perturbation theory:[57]

$$\alpha(\omega) \propto \frac{(\hbar\omega - E_g)^{\nu}}{\hbar\omega}, \tag{13}$$

in which for *direct*, allowed (forbidden) transitions $\nu = \frac{1}{2}$ ($\nu = \frac{3}{2}$) and for *indirect*, allowed (forbidden) transitions $\nu = 2$ ($\nu = 3$). Equation (12) is rewritten as

$$\ln T(\omega) = \ln T_0 - C \frac{(\hbar\omega - E_g)^{\nu}}{\hbar\omega}, \tag{14}$$

and the constants $\ln T_0$, *C*, and E_g are determined from a fit to the spectra near the transmission edge, where no interferences appear yet. In Table VII the obtained parameters are given.

We find that $\nu = 1/2$, i.e., an allowed, direct gap, cannot explain the measured data. Assuming an allowed, *in*direct gap ($\nu = 2$) gave good results for alloys with $z \leqslant 0.7$.

However, for $z \geqslant 0.86$ it is possible to fit the data equally well with $\nu = \frac{3}{2}$, 2, or 3, and with $2.3 < E_g < 2.7$ eV. This large spread is probably due to the fact that the data pertain to polycrystalline films with an hexagonal lattice structure.

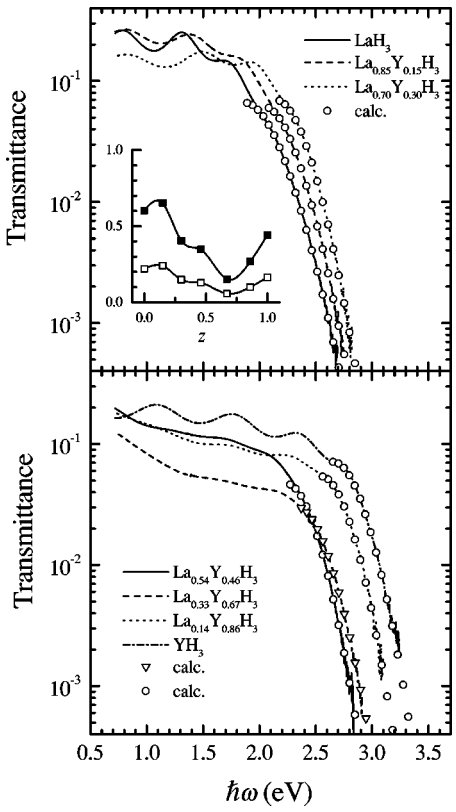

FIG. 24. Measured transmittances (lines) and fitted transmission edges [symbols; see Eq. (14)] for the $La_{1-z}Y_zH_3$ alloys. The inset shows the transmittances of the $La_zY_{1-z}H_3$ alloys 1 eV below the optical gap (see Fig. 25). The open squares are the measured values. Solid symbols are values corrected for the $PdH_{0.7}$ cap layer and the quartz substrate and represent the maximum achievable transmittance of the $La_{1-z}Y_zH_3$ films.

Their optical properties are anisotropic, and therefore the simple formula for $\alpha(\omega)$ is less accurate than for films with $z \leqslant 0.7$, that are cubic thus optically isotropic. To check our assumption we carried out the same fits on transmittance spectra of *epitaxial* YH_3. These films, evaporated on a $CaF_2(111)$ substrate have their *c* axis perpendicular to the surface, and the transmittance is thus measured along one optical axis. Again the best fits were clearly obtained with $\nu=2$ and $E_g=2.659$ eV. From ellipsometry we find for YH_3

TABLE VII. Fit parameters obtained by modeling the transmission edges of $La_{1-z}Y_zH_{3-\delta}$ with Eq. (12) with $\nu=2$. All parameters are dimensionless except E_g, which is in eV.

z	$\ln T_0$	C	E_g	χ^2
0	−2.717	19.65	1.873	0.0028
0.15	−2.792	25.61	2.042	0.0157
0.30	−2.665	29.14	2.150	0.0075
0.46	−3.065	34.29	2.246	0.0062
0.67	−3.502	31.59	2.332	0.0049
0.86	−2.923	38.26	2.551	0.0044
1 (epi)	−2.647	36.33	2.659	0.0007
1 (poly)	−2.374	21.73	2.424	0.0102

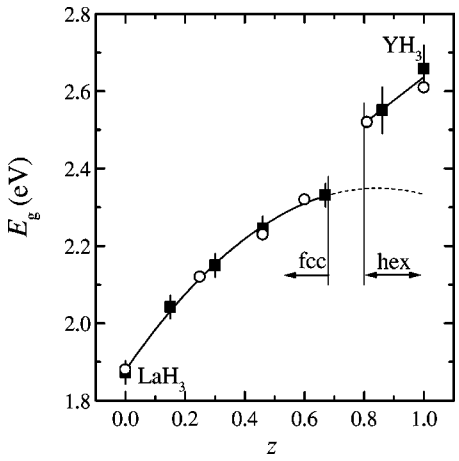

FIG. 25. Optical gap of $La_{1-z}Y_zH_3$ alloys determined by (i) by modeling the transmission edge using Eq. (14) (solid squares), and (ii) by taking the axis cutoff of $\varepsilon_2(\omega)$ in Fig. 23 (open circles). The solid/dashed line is a second-order polynomial fit of the data with $z<0.67$, and suggests an optical gap of 2.32 eV for fcc-YH_3.

$E_g=2.61$ eV (Fig. 23).[58] These values are in good agreement with the calculations of van Gelderen *et al.*[11] who predicted YH_3 to have an optical gap between 2.4 and 2.9 eV.

In Fig. 25 the optical gap as a function of *z* is shown as determined in two different ways. The values are in excellent agreement with each other. The discontinuity between $z=0.67$ and 0.81 coincides with the structural phase transition (as a function of *z*) from fcc to hex (see Fig. 4). For the fcc trihydride region ($z \leqslant 0.67$) the optical gap increases nonlinearly with increasing *z*, and reaches 2.33 eV for $z=0.67$. The shift of E_g is probably a volume effect, because (i) within one phase E_g increases monotonically with decreasing molar volume, and (ii) the discontinuity in $V_m(z)$ coincides with the discontinuity in $E_g(z)$.

6. Polycrystalline vs epitaxial $YH_{3-\delta}$

The trihydride *R-T* spectra of polycrystalline YH_x and of an epitaxial film are compared in Fig. 26. The epitaxial film was grown at high temperature on a $CaF_2(111)$ substrate.[59] Some differences from polycrystalline films are observed. The optical band gap seems slightly larger for the epitaxial film and the interferences in the reflectance have a larger amplitude. Moreover, the reflectance of the polycrystalline film exhibits a downward trend for lower energies, which is not observed for the epitaxial film.

To obtain the dielectric function from the data, the reflectance and transmittance of a multilayer is calculated using the transfer-matrix method.[60] The optical properties of the substrate layer, Al_2O_3 layer, and Pd layer are taken from the literature,[23,61] and the dielectric function of the YH_3 layer is parametrized using Eq. (10), with the Drude term set to zero, because of the insulating nature of the trihydrides.[62] The result of the fit is shown in Fig. 26.

From the fitted $\varepsilon(\omega)$ we calculated the absorption coefficient via

$$\alpha(\omega)=\sqrt{2}\,\frac{\omega}{c}\left[\sqrt{\varepsilon_1^2(\omega)+\varepsilon_2^2(\omega)}-\varepsilon_1(\omega)\right]^{1/2}. \qquad (15)$$

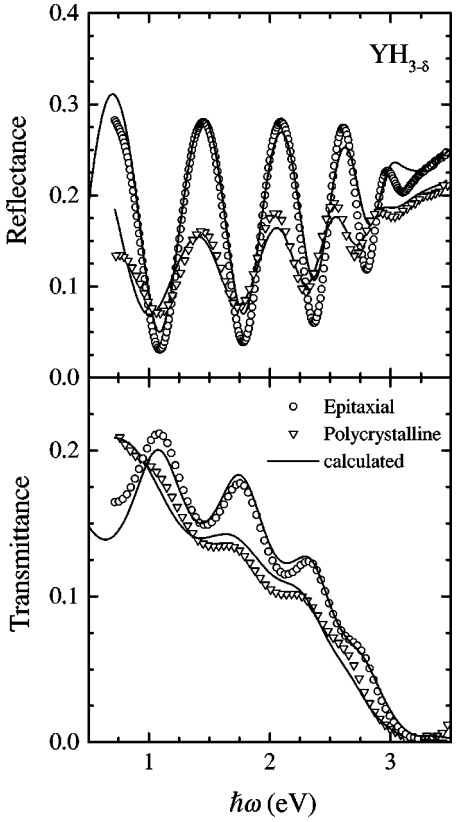

FIG. 26. Reflectance and transmittance of an epitaxial and a polycrystalline $YH_{3-\delta}$ film. Both films are covered with 15-nm Pd. The solid lines are calculated data using a DL parametrization for the parametrization of $\varepsilon(\omega)$.

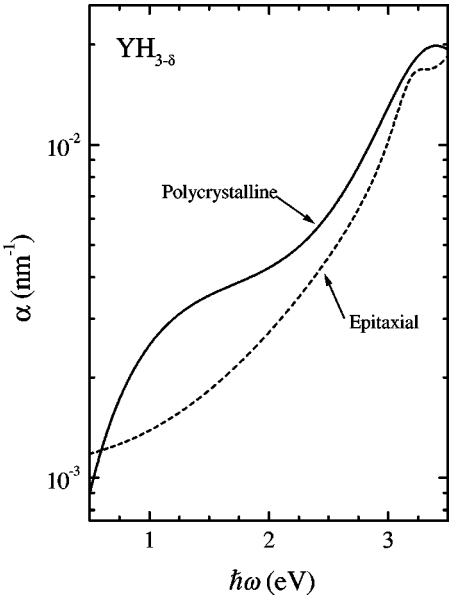

FIG. 27. The absorption coefficient of epitaxial and polycrystalline $YH_{3-\delta}$ obtained from a DL fit of the *R*-*T* spectra (see Fig. 26). In polycrystalline $YH_{3-\delta}$, considerable absorption exists below the optical gap.

Figure 27 shows that the absorption edge is sharper for the epitaxial film. This effect is also seen in other materials, and is often explained by impurity absorptions and is known as the Urbach tail. The difference between the epitaxial and polycrystalline material can also be caused by the optical anisotropy of the hexagonal YH_3. Note that we only probe the optical properties along the *c* axis in the epitaxial case, while we measure a mixture of properties along the *a* axis and the *c* axis in the polycrystalline case. A comparison between polycrystalline and epitaxial LaH_3, which is cubic and therefore isotropic, could give more information on this point.

Figure 27 also shows that the absorption below the optical gap is lower for the epitaxial film. This can also be due to the anisotropy of YH_3. It may also be caused by lattice defects that affect the lattice periodicity and in this way may give rise to optical transitions that are forbidden in the epitaxial case. This supports the results of *GW* calculations on YH_3[11] of a 1-eV dipole forbidden fundamental gap.

IV. CONCLUSIONS

We have determined the structural phase diagram and the optical and electrical properties of the $La_{1-z}Y_zH_x$ system for $x=0$, 2, and 3. We also studied the switching kinetics, thermodynamics, dc resistivity behavior, and optical properties in the regions $2 \lesssim x < 3$, the region where the MI transition takes place.

The structural and optical data reveal that La and Y atoms form a disordered solid solution, and that the alloys do not disproportionate upon hydrogenation. This makes the system a very useful system for studying the nature of the MI transition.

From dc resistivity measurements we observe that LaH_x shows a three-stage hydrogenation for $2<x<3$, whereas all other films show a two-stage hydrogenation. The different stages might be due to hydrogen ordering.

$La_{1-z}Y_z$ films and their hydrides behave in many aspects like their bulk counterparts. The phase diagram for $x=0$, the heat of formation of the trihydride, and optical properties exhibit similar behavior to that of data known for bulk systems. This is what one expects for crystallite sizes of 10–100 nm. The higher resistivity of films compared to bulk values for $x=0$ and 2 are not thin-film effects, but due to the polycrystalline nature of the samples; the electronic mean free paths are of the order of 10 nm for metallic LaH_x and YH_x and therefore much smaller than the film thickness.

Disorder effects are observed throughout the work. They reduce the x-ray coherence length and the free-electron relaxation time, affecting both the dc resistivity as the optical free-electron response. The strong suppression of the dihydride transmission window is also an effect of disorder as well as the lowering of the transmittance of the alloy trihydrides.

$La_{1-z}Y_zH_x$ alloys show a similar MI transition for *x* be-

tween 2 and 3, indicating the robustness of the MI transition-.From this and the optical behavior of the various materials between $x=2$ and 3, we conclude that the MI transition is of electronic nature.

We have been able to determine accurately the optical band gap of $La_{1-z}Y_zH_3$ trihydride alloys. The optical gap increases monotonically with z from 1.87 ± 0.03 eV (orange) for LaH_3 to 2.63 ± 0.03 eV (yellow) for YH_3, and is affected both by the molar volume as the lattice structure. There are indications that the fundamental gap is dipole forbidden and 1–1.8 eV lower than the optical gap. This is in agreement with recent *GW* calculations.

ACKNOWLEDGMENTS

The authors thank S. J. van der Molen, J. W. J. Kerssemakers, M. van den Berg, and B. Dam (VU Amsterdam) and P. A. Duine, P. van der Sluis, R. Coehoorn, and A.-M. Janner (Philips Research) for fruitful discussions. This work was part of the research program of the Stichting voor Fundamenteel Onderzoek der Materie (FOM), financially supported by the Nederlandse Organisatie voor Wetenschappelijk Onderzoek (NWO) and Philips Research, and of the TMR Research Network ''Metal-hydride films with switchable physical properties.''

[1] J. N. Huiberts, R. Griessen, J. H. Rector, R. J. Wijngaarden, J. P. Dekker, D. G. de Groot, and N. J. Koeman, Nature (London) **380**, 231 (1996).
[2] P. van der Sluis, M. Ouwerkerk, and P. A. Duine, Appl. Phys. Lett. **70**, 3356 (1997).
[3] R. Griessen, J. N. Huiberts, M. Kremers, A. T. M. van Gogh;, N. J. Koeman, J. P. Dekker, and P. H. L. Notten, J. Alloys Compd. **253-254**, 44 (1997).
[4] D. G. Nagengast, A. T. M. van Gogh, E. S. Kooij, B. Dam, and R. Griessen, Appl. Phys. Lett. **75**, 2050 (1999).
[5] P. H. L. Notten, M. Kremers, and R. Griessen, J. Electrochem. Soc. **143**, 3348 (1996).
[6] E. S. Kooij, A. T. M. van Gogh, and R. Griessen, J. Electrochem. Soc. **146**, 2990 (1999).
[7] K. K. Ng, F. C. Zhang, V. I. Anisimov, and T. M. Rice, Phys. Rev. Lett. **78**, 1311 (1997); Phys. Rev. B **59**, 5398 (1999).
[8] P. J. Kelly, J. P. Dekker, and R. Stumpf, Phys. Rev. Lett. **78**, 1315 (1997).
[9] R. Eder, H. F. Pen, and G. A. Sawatzky, Phys. Rev. B **56**, 10 115 (1997).
[10] T. Miyake, F. Aryasetiawan, H. Kino, and K. Terakura, Phys. Rev. B **61**, 16 491 (2000).
[11] P. van Gelderen, P. A. Bobbert, P. J. Kelly, and G. Brocks, Phys. Rev. Lett. **85**, 2989 (2000).
[12] F. J. A. den Broeder, S. J. van der Molen, M. Kremers, J. N. Huiberts, D. G. Nagengast, A. T. M. van Gogh, W. H. Huisman, J. P. Dekker, N. J. Koeman, B. Dam, J. H. Rector, S. Plota, M. Haaksma, R. M. N. Hanzen, R. M. Jungblut, P. A. Duine, and R. Griessen, Nature (London) **394**, 656 (1998).
[13] A. T. M. van Gogh, E. S. Kooij, and R. Griessen, Phys. Rev. Lett. **83**, 4614 (1999), and references therein.
[14] K. A. Gschneidner, Jr., and F. W. Calderwood, Bull. Alloy Phase Diagrams **3**, 94 (1982), and references therein.
[15] A. T. M. van Gogh, S. J. van der Molen, J. W. J. Kerssemakers, N. J. Koeman, and R. Griessen, Appl. Phys. Lett. **77**, 815 (2000).
[16] L. J. van der Pauw, Philips Res. Rep. **13**, 1 (1958).
[17] P. Vajda, in *Handbook on the Physics and Chemistry of Rare Earths*, edited by K. A. Gschneidner, Jr. and L. Eyring (Elsevier, Amsterdam, 1995), Vol. 20, p. 207, and references therein.
[18] D. S. Schreiber and R. M. Cotts, Phys. Rev. **131**, 1118 (1963).
[19] J. H. Weaver, R. Rosei, and D. T. Peterson, Phys. Rev. B **19**, 4855 (1979).
[20] J. A. Goldstone, J. Eckert, P. M. Richards, and E. L. Venturini, Solid State Commun. **49**, 475 (1984).
[21] D. Khatamian, W. A. Kamitakira, R. G. Barnes, and D. T. Peterson, Phys. Rev. B **21**, 2622 (1980).
[22] D. L. Anderson, R. G. Barnes, D. T. Peterson, and D. R. Torgeson, Phys. Rev. B **21**, 2625 (1980).
[23] *CRC Handbook of Chemistry and Physics*, 77th ed. (CRC Press, Boca Raton, FL, 1996).
[24] Y. Wang and M. Y. Chou, Phys. Rev. B **44**, 10 339 (1991).
[25] F. H. Spedding, R. M. Valetta, and A. H. Daane, Trans. Am. Soc. Met. **55**, 483 (1962).
[26] K. N. R. Taylor and M. I. Darby, *Physics of Rare Earth Solids* (Chapman and Hall, London, 1972).
[27] T. J. Udovic, Q. Huang, and J. J. Rush, J. Phys. Chem. Solids **57**, 423 (1996).
[28] A. Remhof, G. Song, Ch. Sutter, A. Schreyer, R. Siebrecht, H. Zabel, F. Güthoff, and J. Windgasse, Phys. Rev. B **59**, 6689 (1999).
[29] Y. Wang and M. Y. Chou, Phys. Rev. B **49**, 10 731 (1994).
[30] A. T. M. van Gogh, D. G. Nagengast, E. S. Kooij, N. J. Koeman, and R. Griessen, Phys. Rev. Lett. **85**, 2156 (2000).
[31] E. S. Kooij, A. T. M. van Gogh, D. G. Nagengast, and R. Griessen, Phys. Rev. B **62**, 10 088 (2000).
[32] J. P. Dekker, J. van Ek, A. Lodder, and J. N. Huiberts, J. Phys.: Condens. Matter **5**, 48 055 (1993).
[33] Y. Wang and M. Y. Chou, Phys. Rev. Lett. **71**, 1226 (1993).
[34] Y. Wang and M. Y. Chou, Phys. Rev. B **51**, 7500 (1995).
[35] P. Scherrer, Gött. Nachrichten **2**, 98 (1918).
[36] W. M. Mueller, J. P. Blackledge, and G. G. Libowitz, Metal Hydrides (Academic Press, New York, 1968).
[37] P. R. Lacher, Proc. R. Soc. London, Ser. A **161**, 525 (1938); Proc. Cambridge Philos. Soc. **34**, 518 (1938).
[38] *The Metal-Hydrogen System*, edited by Y. Fukai (Springer-Verlag, Berlin, 1993).
[39] R. Feenstra, R. Brouwer, and R. Griessen, Europhys. Lett. **7**, 425 (1988).
[40] R. C. Brouwer and R. Griessen, Phys. Rev. B **40**, 1481 (1989).
[41] A. E. Curzon and O. Singh, Thin Solid Films **57**, 157 (1979).
[42] G. S. Fleming, S. H. Liu, and T. E. Loucks, Phys. Rev. Lett. **21**, 1524 (1968).
[43] S. L. Altmann and C. J. Bradley, Proc. Phys. Soc. London **92**, 764 (1967).

[44] D. J. Peterman, B. N. Harmon, J. Marchiando, and J. H. Weaver, Phys. Rev. B **19**, 4867 (1979).
[45] F. Wooten, *Optical Properties of Solids* (Academic Press, New York, 1972).
[46] E. Fromm, Z. Phys. Chem., Neue Folge **147**, 61 (1986); E. Fromm, H. Uchida, and B. Chelluri, Ber. Bunsenges. Phys. Chem. **87**, 410 (1983).
[47] S. J. van der Molen, J. W. J. Kerssemakers, J. H. Rector, N. J. Koeman, B. Dam, and R. Griessen, J. Appl. Phys. **86**, 6107 (1999).
[48] J. H. Weaver and D. W. Lynch, Phys. Rev. B **7**, 4737 (1973).
[49] J. H. Weaver and C. G. Olson, Phys. Rev. B **15**, 590 (1977).
[50] D. E. Eastman, Solid State Commun. **7**, 1697 (1966).
[51] O. Wiener, Abh. Math. Phys. Kl. König. Sächs. Ges. **32**, 509, 1912.
[52] This conclusion is premature, because Wiener bounds are valid for materials that are optically isotropic. However, the conclusion turns out to be correct after analyzing the isotropic dihydrides.
[53] J. H. Weaver, D. T. Peterson, and R. L. Benbow, Phys. Rev. B **20**, 5301 (1979).
[54] D. J. Peterman, J. H. Weaver, and D. T. Peterson, Phys. Rev. B **23**, 3903 (1981).
[55] W. A. Harrison, *Electronic Structure and the Properties of Solids* (Freeman, San Francisco, 1980).
[56] The mechanism is similar to that proposed by Peterman *et al.*, based on optical measurements on *bulk* LaH_x (Ref. 54).
[57] E. J. Johnson, in *Absorption Near the Fundamental Edge, Semiconductors and Semimetals*, Vol. 3, edited by R. K. Willardson and C. Beer (Academic Press, New York, 1967).
[58] Earlier we reported an optical gap for YH_3 of 2.8 eV (Ref. 13). This value was obtained from data on polycrystalline films, and is therefore less accurate than the value 2.63 ± 0.03 eV presented here.
[59] D. G. Nagengast, J. W. J. Kerssemakers, A. T. M. van Gogh, B. Dam, and R. Griessen, Appl. Phys. Lett. **75**, 1724 (1999).
[60] M. Born and E. Wolf, *Principles of Optics*, 6th ed. (University Press, Cambridge, 1980).
[61] *Handbook of Optics*, edited by M. Bass, E.W. van Stryland, D.R. Williams, and W.L. Wolfe (McGraw-Hill, New York, 1995), Vol. II.
[62] Because hydrogen vacancies in the substriochiometric trihydrides act as electron donors, a nonzero plasma frequency is expected. Indeed Lee and Shin (Ref. 63) observed a Drude-like free-electron contribution in the optical constants of $YH_{3-\delta}$, but with a plasma frequency of 0.16 eV, which is outside our measurement region.
[63] M. W. Lee and W. P. Shin, J. Appl. Phys. **86**, 6798 (1999).